Laser-driven lepton polarization in the quantum radiation-dominated reflection regime

Kai-Hong Zhuang,[1] Yue-Yue Chen,[1,*] Yan-Fei Li,[2,†] Karen Z. Hatsagortsyan,[3,‡] and Christoph H. Keitel[3]

[1]*Department of Physics, Shanghai Normal University, Shanghai 200234, China*
[2]*Department of Nuclear Science and Technology, Xi'an Jiaotong University, Xi'an 710049, China*
[3]*Max-Planck-Institut für Kernphysik, Saupfercheckweg 1, 69117 Heidelberg, Germany*

(Received 9 May 2023; accepted 11 July 2023; published 1 August 2023)

Generation of ultrarelativistic polarized leptons during interaction of an ultrarelativistic electron beam with a counterpropagating ultraintense laser pulse is investigated in the quantum radiation-dominated domain. While the symmetry of the laser field tends to average the radiative polarization of leptons to zero, we demonstrate the feasibility of sizable radiative polarization through breaking the symmetry of the process in the reflection regime. After the reflection, the off-axis particles escape the tightly focused beam with polarization correlated to the emission angle, while the particles at the beam center are more likely to be captured in the laser field with unmatched polarization and kinetic motion. Meanwhile, polarization along the electric field emerges due to the spin rotation in the transverse plane via precession. In this way, the combined effects of radiative polarization, spin precession, and the laser field focusing are shaping the angle-dependent polarization for outgoing leptons. Our spin-resolved Monte Carlo simulations demonstrate an angle-dependent polarization degree up to ∼20% for both electrons and positrons, with a yield of one pair per seed electron. It provides a new approach for producing polarized high density electron and positron jets at ultraintense laser facilities.

DOI: 10.1103/PhysRevD.108.033001

I. INTRODUCTION

Polarized electrons and positrons are valuable investigation tools in nuclear and high-energy physics [1,2]. They are indispensable for high-energy experiments in the next generation of colliders, which are aiming to search for physics beyond the standard model [3].

There are standard methods for polarization of relativistic electron beams: illuminating a photocathode by circularly polarized light [4], or by radiative polarization in a storage ring via the Sokolov-Ternov effect [5–7]. Since antiparticles are not available in the matter, generating intensely polarized positrons is more challenging than polarized electrons. It is well known that β-decay of specific radioisotopes can produce polarized positrons [8], however, the quality of the beam is far from practical usage. So far, there are mainly two possible approaches to generate intensely polarized positrons for high-energy physics [9]. One is the so-called undulator based positron source [10], producing circularly polarized γ-photons via electron radiation in a helical undulator, and then converting it to electron-positron pairs in a tungsten target. The proof-of-principle E166 experiment was performed at Stanford Linear Accelerator Center. The positrons of $2–6 \times 10^4$/pulse are produced with longitudinal polarization above 80% at an energy of about 6 MeV [11]. Alternatively, γ-photons can be generated by Compton backscattering of a circularly polarized laser [12]. In the second method proposed in the Thomas Jefferson National Accelerator Facility, which is termed Polarized Electrons for Polarized Positrons, the polarized positrons are produced using bremsstrahlung radiation of polarized electrons [13]. However, upgrading the intensity of the positron source to meet the requirement of future electron-positron colliders (2.82×10^{14} s^{-1}) is still an extremely challenging task [14].

With the invention of chirped-pulse amplification and optical parametric chirped-pulse amplification laser techniques, the current laser intensity is already able to reach 10^{23} W/cm^2 [15], and an increase up to 10^{25} W/cm^2 is expected in next-generation laser facilities [16–20]. Strong lasers have been applied for generating electron-positron jets via laser-solid interaction [21–24], as well as via laser-electron beam interaction [25].

Spin effects in nonlinear QED processes in strong laser fields have been investigated theoretically, in particular, in

*yue-yue.chen@shnu.edu.cn
†liyanfei@xjtu.edu.cn
‡k.hatsagortsyan@mpi-hd.mpg.de

multiphoton Compton scattering [26–33], in Kapitz-Dirac scattering [34–36], in the multiphoton Breit-Wheeler process (pair production) [37–39], as well as in the multiphoton Bethe-Heilter process in a Coulomb field [40]. However, these studies have mostly addressed the processes in a plane-wave field and/or not ultraintense field regimes. In an ultrastrong laser field, the strong-field QED effects are well described within the local constant field approximation (LCFA) [41,42]. An efficient formalism based on LCFA describing polarization effects during a photon emission and pair production in background strong fields has been developed by Baier and Katkov [6,41,43].

When an unpolarized electron radiates in a strong external field, the electron spin after the emission is preferentially oriented opposite to the magnetic field in the electron rest frame, which is the energetically most favorable state. This effect is termed radiative polarization [5,6]. Similarly, during pair creation of a linearly polarized/unpolarized photon in a strong external field, the electron (positron) spin favors the opposite (same) direction with respect to the magnetic field (in the electron rest frame), which may lead to the polarization of electron-positron pairs [41]. The polarization effect is significantly larger in the case of a pair production process than in that for photon emission. This is because of the larger asymmetry of the pair production probability between the final spin-up and -down states in a constant field, compared with that of radiation. Available ultrastrong laser fields put forward a desire to exploit intense fields for radiative or pair production polarization of electron (positron) beams. However, its straightforward realization is not possible. In fact, a laser field represents a quite remarkable symmetric field, with the negative and positive half-cycles inducing opposite spin effects. Even in an ultrashort laser field, the field asymmetry is too weak to allow a significant polarization, e.g., the polarization is less than 8% in a single cycle plane wave laser pulse discussed in [33]. Therefore, essentially asymmetric laser fields are required to polarize particles either with radiative or pair production polarization. In [44,45] a model asymmetric laser field is devised in the form of a strong rotating electric field, which not surprisingly yields a large electron radiative polarization, reviving the idea to seek radiative (pair production) polarization in more realistic field configurations.

Recently, we have developed a fully polarization resolved Monte Carlo method [46–48] for investigations of spin effects in nonlinear QED processes in ultrastrong focused laser fields, using spin-resolved radiation and pair production probabilities in LCFA, calculated with the Baier-Katkov operator method [41,49]. Employing this method, we proposed a new concept of producing polarized positrons with strongly focused two-color laser pulses [50], see also [51]. The asymmetry of the two-color laser field allows for polarization of pairs up to ∼60% with an efficiency of 10^{-2} positrons per electron. Further, with a fine-tuning of the ellipticity of the laser field, the polarized particles arising from different laser cycles can be separated due to spin-dependent radiation reaction, which promotes a further enhancement of polarization [46,52,53]. The positron's density can be further increased to 30 nC by using laser-solid interaction [54], or to 10^5–10^6/bunch by using initially polarized electrons [48]. It also has been proposed to produce polarized leptons via phase-matched radiation reactions between particle momentum and polarization [48,55,56], followed by the postselection technique discussed in detail in Ref. [56]. In another recent development, the electron and photon polarization generated in strong fields in plasma has been employed as a diagnostic tool to

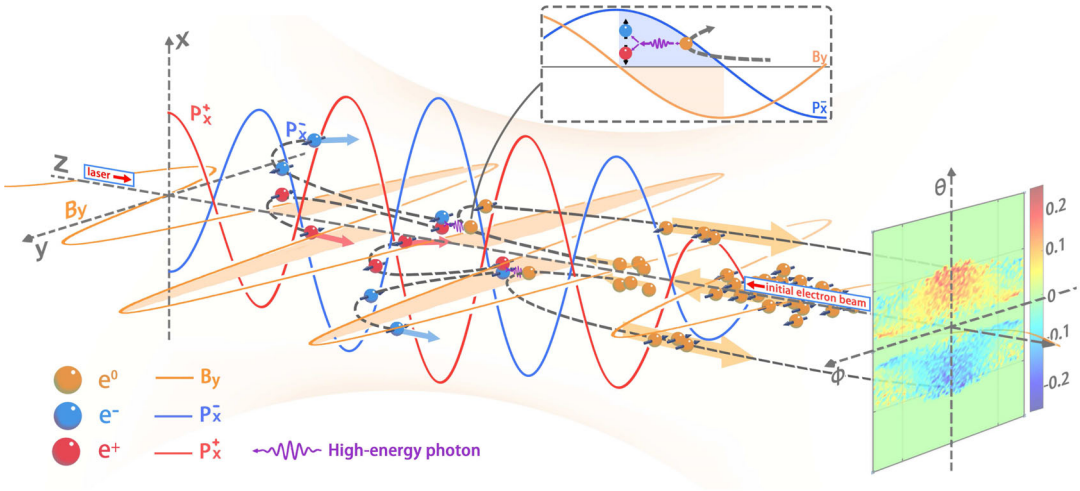

FIG. 1. Scheme of laser-based polarized positron beam production. An intense linearly polarized laser pulse head-on collides with an unpolarized relativistic electron beam, resulting in emission of γ photons in forward direction, which decay into electron-positron pairs. The produced pairs are reflected in the laser field and polarized with spin parallel and antiparallel to magnetic field direction for polar angle $\theta > 0$ and $\theta < 0$, respectively.

monitor transient magnetic fields in plasma [57,58], or characterize the ultrarelativistic plasma instabilities [59].

In this paper, we investigate an intense laser beam interaction with a counterpropagating electron beam. Although the applied laser beam is well symmetric, we aim to obtain asymmetric electron-laser field interaction and generate spin polarization of seed electrons and created pairs via invoking the reflection regime of the interaction [60,61], see the scheme in Fig. 1. Especially advantageous for the creation of asymmetric laser-electron interaction is the applied quantum radiation-dominated regime (QRDR). Our simulation shows that both the reflected seed electrons and pairs are polarized in the intense symmetric field in the reflection regime strengthened with QRDR. The correlation between the cycle-dependent radiative polarization and the reflection angle gives rise to the angle-dependent polarization of particles in a tightly focused symmetric laser field. The physical picture of the interaction and emerging polarization are analyzed in detail.

The QRDR is characterized by the following large parameters: $\chi_e \gtrsim 1$, and $\alpha a_0 \gtrsim 1$ [62]. Here, the classical strong field parameter is $a_0 = eE_0/m\omega$, and the quantum strong field parameter $\chi_e = |e|\sqrt{|F_{\mu\nu}p^\nu|^2}/m^3$ [42], with the electron charge $-e$ and mass m, the laser field tensor $F_{\mu\nu}$, the field amplitude E_0 and frequency ω, and the electron four-momentum p^ν (the relativistic units $\hbar = c = 1$ are used).

Our paper is organized as follows. Section II presents the general semiclassical simulation method of spin-resolved laser-electron interaction. The spin-resolved photon emission and pair production probabilities, as well as the definition of the instantaneous quantization axes for simulations, are given in this section. The results of the numerical simulation are presented in Sec. III, and the polarization for both reflected seed electrons and produced pairs are investigated. A discussion on how the radiative polarization and the focusing effect of the laser field determine the angle-dependent polarization of seed electrons is presented in Sec. III A. The polarization of particles arising from pair creation is analyzed in Sec. III B. Our conclusion is given in Sec. V. The details on the numerical method for nonlinear Compton scattering and nonlinear Breit-Wheeler process are provided in the Appendices A and B, respectively.

II. SIMULATION METHOD

Recently, a semiclassical Monte Carlo method was developed to describe the electron (positron) spin-resolved dynamics in nonlinear QED processes in ultrastrong laser fields [46–48,50,52,55,63]. The photon emissions and pair productions are simulated via Monte Carlo algorithm using spin-resolved quantum probabilities. Between photon emissions and after the pair production, the electron's (positron's) motion in the external field is governed by the Lorentz force, while spin precession is described by Bargmann-Michel-Telegdi (BMT) equation [64,65].

The spin-resolved photon emission and pair production probabilities are derived with the QED operator method in LCFA [41,49]. After summing over the polarization of emitted photons, we obtain the probability for emitting a photon with an energy ω during time step Δt:

$$
\begin{aligned}
dW^R(\boldsymbol{\zeta},\boldsymbol{\zeta}') &= \frac{1}{2}(a + \boldsymbol{b}\cdot\boldsymbol{\zeta}') \\
a &= C_0 d\omega \left\{ \frac{\varepsilon^2+\varepsilon'^2}{\varepsilon'\varepsilon} \mathrm{K}_{\frac{2}{3}}(z_q) - \int_{z_q}^{\infty} dx \mathrm{K}_{\frac{1}{3}}(x) \right. \\
&\quad \left. - \frac{\omega}{\varepsilon}\boldsymbol{\zeta}\cdot\mathbf{b}\mathrm{K}_{\frac{1}{3}}(z_q) \right\}, \\
\boldsymbol{b} &= C_0 d\omega \left\{ \left[2\mathrm{K}_{\frac{2}{3}}(z_q) - \int_{z_q}^{\infty} dx \mathrm{K}_{\frac{1}{3}}(x) \right] \boldsymbol{\zeta} - \frac{\omega}{\varepsilon'} \mathrm{K}_{\frac{1}{3}}(z_q)\mathbf{b} \right. \\
&\quad \left. + \frac{\omega^2}{\varepsilon'\varepsilon} \left[\mathrm{K}_{\frac{2}{3}}(z_q) - \int_{z_q}^{\infty} dx \mathrm{K}_{\frac{1}{3}}(x) \right] (\boldsymbol{\zeta}\cdot\hat{\mathbf{v}})\hat{\mathbf{v}} \right\},
\end{aligned} \tag{1}
$$

where $\boldsymbol{\zeta}$ and $\boldsymbol{\zeta}'$ are the spin polarization vectors before and after the emission, ε and ε' electron energies, $z_q = \frac{2}{3\chi_e}\frac{\omega}{\varepsilon'}$ with χ_e controlling the magnitude of quantum effects, $C_0 = \frac{\alpha}{\sqrt{3}\pi\gamma^2}$, $\mathbf{b} = \hat{\mathbf{v}} \times \boldsymbol{s}$ with $\hat{\mathbf{v}}$ and $\boldsymbol{s}$ being unit vectors along the direction of electron velocity and acceleration, respectively. The final polarization vector of the electron resulting from the scattering process itself is $\boldsymbol{\zeta}_f^R = \frac{\boldsymbol{b}}{a}$, which is the quantization axis for radiation adopted in our Monte Carlo simulations. After each photon emission, the spin of the emitting particle is either parallel or antiparallel to $\boldsymbol{n}^R = \boldsymbol{\zeta}_f^R$ using the common stochastic algorithm. If a photon emission event is rejected, then one should be aware that the spin of electrons between emissions should be also changed since no-emission probability W^{NR} also has a dependency on initial electron spin [48]:

$$
\begin{aligned}
W^{NR}(\boldsymbol{\zeta},\boldsymbol{\zeta}') &= \frac{1}{2}(c + \boldsymbol{\zeta}'\cdot\boldsymbol{d}), \\
c &= 1 - \int_0^{\varepsilon} \tilde{F}_0 d\omega \Delta t, \\
\boldsymbol{d} &= \boldsymbol{\zeta}\left(1 - \int_0^{\varepsilon} \bar{F}_0 d\omega \Delta t\right) \\
&\quad + \mathbf{b}C_0 \int_0^{\varepsilon} \frac{\omega}{\varepsilon} \mathrm{K}_{\frac{1}{3}}(z_q) d\omega \Delta t,
\end{aligned} \tag{2}
$$

where

$$\tilde{F}_0 = C_0 d\omega \left\{ \frac{\varepsilon^2+\varepsilon'^2}{\varepsilon'\varepsilon} \mathrm{K}_{\frac{2}{3}}(z_q) - \int_{z_q}^{\infty} dx \mathrm{K}_{\frac{1}{3}}(x) - \frac{\omega}{\varepsilon} \boldsymbol{\zeta} \cdot \mathbf{b} \mathrm{K}_{\frac{1}{3}}(z_q) \right\},$$

$$\bar{F}_0 = C_0 d\omega \left\{ \frac{\varepsilon^2+\varepsilon'^2}{\varepsilon'\varepsilon} \mathrm{K}_{\frac{2}{3}}(z_q) - \int_{z_q}^{\infty} dx \mathrm{K}_{\frac{1}{3}}(x) \right\}.$$

The no-emission probabilities $W_{\uparrow}^{NR}$ and $W_{\downarrow}^{NR}$ are asymmetric with respect to an arbitrary quantization axis $\boldsymbol{e}$. Consequently, between photon emissions, the electron spin state along $\boldsymbol{e}$ changes to $\zeta_f^e = \frac{W^{NR}(\boldsymbol{e})-W^{NR}(-\boldsymbol{e})}{W^{NR}(\boldsymbol{e})+W^{NR}(-\boldsymbol{e})} = \frac{\boldsymbol{e}\cdot\boldsymbol{d}}{c}$. Therefore, the final polarization vector without radiation is given by the above expression with $\boldsymbol{e}$ taken away, i.e. $\boldsymbol{\zeta}_f^{\boldsymbol{NR}} = \frac{\boldsymbol{d}}{c}$. In Monte Carlo simulations, the spin of an electron between emissions collapses to one of the two pure states $\pm\boldsymbol{n}^{NR}$ with $\boldsymbol{n}^{NR} = \boldsymbol{\zeta}_f^{NR}/|\boldsymbol{\zeta}_f^{NR}|$ using random numbers. Note that, the polarization between emissions is physically related to radiative correction [55,66]. Afterwards the spin precession follows the BMT equation until the next step.

The emitted photons can further produce electron-positron pairs while propagating in the intense laser field. After averaging over the polarization of the electrons, the spin-resolved pair production probability of producing an electron with energy ε_- and positron ε_+ reads [49]:

$$\begin{aligned} dW^P(\boldsymbol{\xi},\boldsymbol{\zeta}^+) &= \frac{1}{2}(a_+ + \boldsymbol{b}_+ \cdot \boldsymbol{\zeta}^+) \\ a_+ &= \bar{C}_0 d\varepsilon \left\{ \int_{z_p}^{\infty} dx \mathrm{K}_{\frac{1}{3}}(x) + \frac{\varepsilon^2+\varepsilon_+^2}{\varepsilon\varepsilon_+} \mathrm{K}_{\frac{2}{3}}(z_p) \right. \\ &\quad \left. - \xi_3 \mathrm{K}_{\frac{2}{3}}(z_p) \right\}, \\ \boldsymbol{b}_+ &= \bar{C}_0 d\varepsilon \left\{ \xi_1 \mathrm{K}_{\frac{1}{3}}(z_p) \frac{\omega}{\varepsilon_+} \mathbf{s} + \xi_2 \hat{\mathbf{v}} \left(-\frac{\omega}{\varepsilon} \int_{z_p}^{\infty} dx \mathrm{K}_{\frac{1}{3}}(x) \right. \right. \\ &\quad \left. \left. + \frac{\varepsilon_+^2-\varepsilon^2}{\varepsilon\varepsilon_+} \mathrm{K}_{\frac{2}{3}}(z_p) \right) + \left(\frac{\omega}{\varepsilon} - \xi_3 \frac{\omega}{\varepsilon_+} \right) \mathbf{b} \mathrm{K}_{\frac{1}{3}}(z_p) \right\}. \end{aligned} \tag{3}$$

Here $\bar{C}_0 = \frac{\alpha m^2}{\sqrt{3}\pi\omega^2}$, $z_p = \frac{2}{3\chi_\gamma}\frac{\omega^2}{\varepsilon_+\varepsilon_-}$, $\boldsymbol{\zeta}^+$ and $\boldsymbol{\xi} = (\xi_1, \xi_2, \xi_3)$ are the spin polarization vectors of a produced positron and stokes parameters of a parent photon, respectively. The quantum parameter for pair production is $\chi_\gamma = |e|\sqrt{(F_{\mu\nu}k^\nu)^2}/m^3$, with electron four-momentum $k = (\omega, \boldsymbol{k})$ of the incoming γ-photon. The instantaneous spin quantization axis for pair production is along $\boldsymbol{\zeta}_f^+ = \frac{\boldsymbol{b}_+}{a_+}$. If the photon is linearly polarized with $\boldsymbol{\xi} = (0, 0, \xi_3)$ or unpolarized, then $\boldsymbol{\zeta}_f^+$ becomes the magnetic field direction in the frame of the center-of-mass of the produced pairs. The polarization of the produced pairs is decided by probability of Eq. (3) within the Monte Carlo algorithm. After the pair is produced, the parent γ-photon is removed from the simulation, and the created particles can further emit photons and again produce pairs, which could lead to a cascade in the case of large χ_e. In a similar manner, photon polarization has also been included in the simulation (see more details in [47,48,63]).

III. RESULTS AND ANALYSIS

In this section, we present the results of our Monte Carlo simulations. We consider an ultrarelativistic electron beam with energy $\varepsilon_0 = 1.3$ GeV colliding with a tightly-focused linearly polarized strong laser field with intensity $a_0 = 760$ ($I \sim 10^{24}$ W/cm^2), see the scheme in Fig. 1. In the simulation the electrons move in a given laser field. The laser pulse duration is $\tau_p = 3T$ with T being the laser period, beam waist $w_0 = 2\lambda_0$, and wavelength $\lambda_0 = 1$ μm. The electron beam in the simulation consists of $\sim 10^6$ electrons that have a uniform distribution in the longitudinal direction and a Gaussian distribution in the transverse direction. The length of the electron beam is $L_e = 1.5\lambda_0$, and the radius $r_e = \lambda_0$. The angular spreading of the electron beam is $\Delta\theta = 1$ mrad, and the energy spreading $\Delta\varepsilon/\varepsilon = 0.02$, which are typical for laser wakefield acceleration of electrons [67]. The parameters are chosen such that the interaction is in the QRDR, when $\chi_e \approx 2a_0(\omega/m)\gamma > 1$ and $\alpha a_0 \chi_e > 1$, with the electron effective energy in the laser field $\varepsilon = m\gamma$. In addition, the electrons experience a large energy loss, positrons are produced with high density, and reflection occurs as $a_0/2 > \gamma$, which breaks the symmetry of the interaction. Note that due to large radiation losses, the electron energy in the laser field ε is significantly smaller than ε_0. The specific choice of the laser and electron parameters is to allow the electrons to be reflected near the laser pulse peak.

A. Radiative polarization of seed electrons

The angular distribution and polarization of seed electrons after the interaction are presented in Fig. 2. The strong interaction induces a large number of photon emissions, more than one photon per laser cycle $N_\gamma \sim \alpha a_0 \gtrsim 1$ [60]. The electrons with considerable energy loss could be reflected when the external field exerts a Lorentz force along the laser propagation direction. In the considered reflection regime, after the interaction, the seed electrons move in the reflection direction $|\theta| = |\cos^{-1}(p_z/\gamma)| < 90^0$ (θ is the polar angle between the particle momentum and the laser propagation direction), as shown in Fig. 2(c). Interestingly, the seed electrons are transversely polarized with the highest polarization degree around 20%. Along the laser polarization direction (x-axis), the electrons are polarized with central symmetry, see Fig. 2(a). For $\theta > 20^\circ$ ($\theta < -20^\circ$), ζ_x is positive at $\phi < 0$ ($\phi > 0$) and

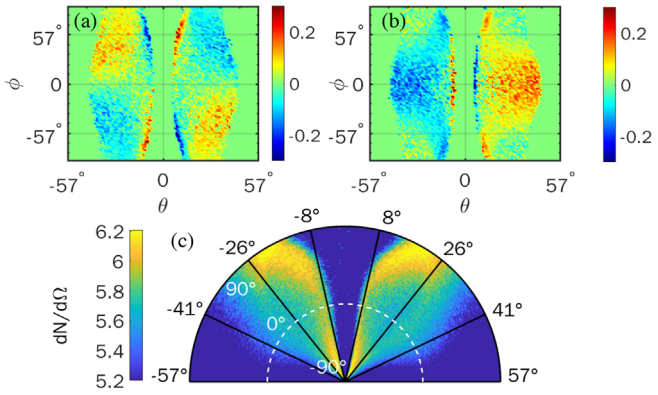

FIG. 2. The averaged polarization distribution (a) ζ_x, (b) ζ_y, and (c) angular distribution $d^2N/d\Omega$ vs the polar angle θ (degree, black scale) and azimuthal angle ϕ (degree, white scale) for seed electrons after the interaction at $t = 20T$.

negative at $\phi > 0$ ($\phi < 0$). Meanwhile, polarization along the magnetic field direction (y-axis) is opposite with regard to $\theta = 0$, see Fig. 2(b). The electrons with $\theta < 0$ have negative ζ_y while those with $\theta > 0$ have positive ζ_y. It is worth noting that the polarization direction in the small angle region ($|\theta| \lesssim 20°$) is opposite to that in the large angle region ($|\theta| \gtrsim 20°$).

1. Large angle electrons: Polarization along the magnetic field

In the investigation of the angle-dependent polarization, we start with the analysis of the electron dynamics. We calculate the average momentum evolution and the trajectories for electrons with $\theta > 20°$ and $\theta < -20°$, respectively (see Fig. 3). On average, the electrons with final momentum $p_x^f > 0$ and $p_x^f < 0$ are initially distributed with $\bar{x}(0) = \pm\lambda_0/2$, respectively. Generally, the electrons are reflected due to the damping in z-motion induced by radiation reaction and further acceleration in the laser propagation direction induced by the Lorentz force. Defining the reflection point in terms of the laser phase by $\bar{p}_z = 0$, the electrons initially distributed at $\bar{x}(0) = \pm\lambda_0/2$ are reflected at the laser phase $\varphi/2\pi = 4.2$ and $\varphi/2\pi = 4.1$, respectively [see Fig. 3(a)].

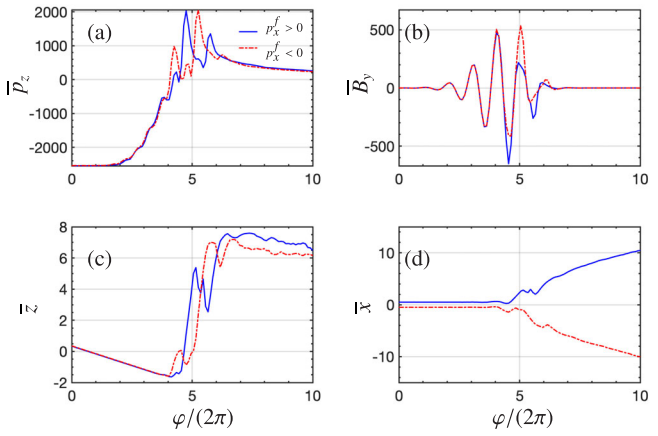

FIG. 3. The electron dynamics vs the laser phase $\varphi/2\pi$: (a) $\bar{p}_z$ normalized to m, (b) magnetic field $\bar{B}_y$ normalized to $m\omega/|e|$, (c) trajectory $\bar{z}$ and (d) $\bar{x}$, normalized to λ_0. The overline indicates averaging over electrons within $(\theta, \phi) \in [-20°, 20°]$ for the final momentum $p_x^f > 0$ (blue solid line) and $p_x^f < 0$ (red dashed line).

In the case of $a_0 \gg 1$, the reflected electrons become ultrarelativistic along the laser propagation direction within the laser quarter cycle due to the Lorentz force effect. Because of the ultrarelativistic drift in the laser propagation direction, the electron dephasing time with respect to the laser field is much longer than the laser period. At the same time, the electrons are transversely pushed away from the beam axis by the ponderomotive potential of the tightly focused laser field. As illustrated in Figs. 3 and 4, the electrons initially distributed at $\bar{x}(0) = \lambda_0/2$ are accelerated to $p_z \sim 2 \times 10^3$ in the acceleration cycle $4.55 < \varphi/2\pi < 4.8$ [Fig. 3(a)] and stay in this cycle for a long time until they slowly drift to the deceleration cycle $4.8 < \varphi/2\pi < 5.05$ [Fig. 4]. During the phase-matched motion at $4.55 < \varphi/2\pi < 5.05$, the transverse coordinate $\bar{x}$ increases up to $2.6\lambda_0$ [Fig. 3(d)] because $\bar{p}_x$ remains positive [Fig. 4]. As the employed laser field is short, during the phase-matched motion, the electrons travel half of the Rayleigh length of the laser beam [$\bar{z}$ reaches to $5\lambda_0$, see Fig. 3(c)], where the field intensity is significantly reduced. After they further drift to the next half-cycle $5.05 < \varphi/2\pi < 5.55$, the laser field attempts to pull the electrons back towards the beam center. However, the rather

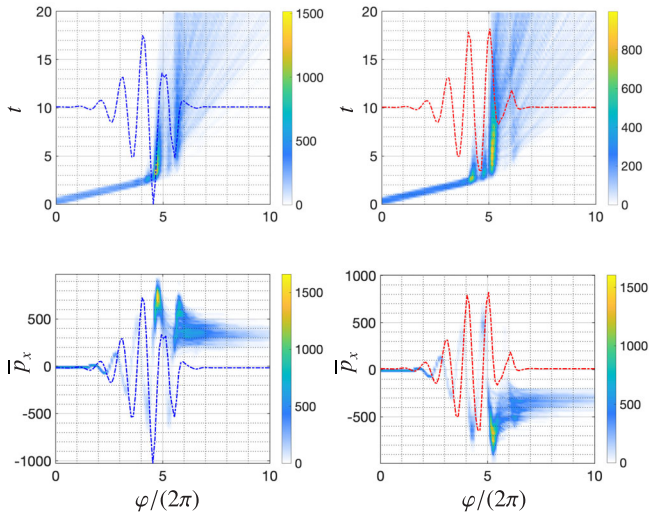

FIG. 4. (Upper row) The number density $d^2N/(dtd\varphi)$ versus evolution time t/T and phase $\varphi/2\pi$, and (bottom row) the number density $d^2N/(dp_xd\varphi)$ versus p_x and $\varphi/2\pi$: for electrons with final momentum $p_x^f > 0$ (left column) and $p_x^f < 0$ (right column). The electrons are within $(\theta, \phi) \in [-20°, 20°]$. The superimposed dot-dashed lines are the corresponding magnetic fields.

weak field [Fig. 3(b)] could not flip the sign of $\bar{p}_x$. Eventually, the electrons are scattered out of the beam in the transverse direction [see Figs. 3(c) and 3(d) where $\bar{x}$ is increasing, while $\bar{z}$ is decreasing at $\varphi/2\pi > 6$]. In our stochastic simulation, some electrons directly fly out of the laser beam at the half-cycle $4.55 < \varphi/2\pi < 5.05$. Those are the electrons with linear time dependence on the phase until $20T$ [Fig. 4] and having a constant p_x after $\varphi/2\pi = 5.05$ [Fig. 4]. However, most of the electrons are scattered out of the beam at $5.55 < \varphi/2\pi < 6.05$ [Fig. 4 (left column)].

Thus, the electron dynamics is mostly determined by the half-cycles near the pulse peak, which could exert a strong transverse acceleration to push the electrons out of the laser beam. For electrons distributed with $x(0) > 0$, p_x^f is mainly affected by the negative half-cycle peaked at $\varphi/2\pi = 5.55$, which catches the electrons in the acceleration phase of p_z and provides strong transverse acceleration along $x > 0$, pushing the electrons further away from the beam center. Due to the features of the focused laser beam, the effects of the next positive half-cycle on the electron's motion cannot cancel out that from the previous negative half-cycle. Similarly, the dynamics of electrons distributed with $x(0) < 0$ is mainly determined by the positive half-cycle peaked at $\varphi/2\pi = 5.05$, which catches the electrons in the acceleration phase of p_z and exerts a strong negative transverse acceleration [Fig. 4 (right column)].

With the information on the electron dynamics at hand, we proceed to interpret the correlation of momentum and polarization (see Fig. 5). After the reflection at $\varphi/2\pi = 4.2$, the electrons with $\bar{x}(0) > 0$ are accelerated and are phase matched by the main negative half-cycle peaked at $\varphi/2\pi = 4.55$, where the electron's average quantum strong-field parameter $\bar{\chi}_e$ is large [Fig. 5(c)], and the electrons emit a considerable amount of photons [Fig. 5(b)] with a significant recoil due to the large $\bar{\chi}_e$. This leads to polarization of electrons antiparallel with the magnetic field direction, i.e. $B_y < 0$, $\zeta_y > 0$. After the main negative peak, χ_e (spin effects) and emission times are both suppressed due to copropagation geometry and weakened fields [Fig. 5(c)], consequently $\bar{\zeta}_y$ is relatively constant after $\varphi/2\pi = 4.55$ [Fig. 5(a)]. Similarly, the electrons with $\bar{x}(0) < 0$ are accelerated by the main positive half-cycle peaked at $\varphi/2\pi = 5.05$, where the electrons are radiatively polarized with $\zeta_y < 0$ [see Fig. 5(b)]. Therefore, we conclude that the polarization, similar to the electron motion, is also mostly determined by the main acceleration half-cycle, leading to the correlation of ζ_y and p_x.

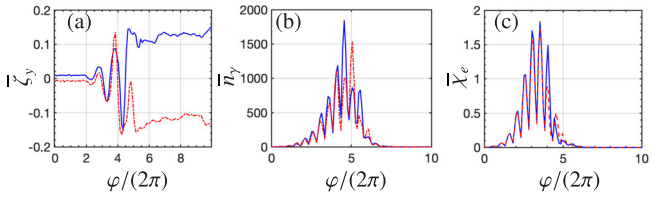

FIG. 5. The evolution of y-component polarization $\bar{\zeta}_y$ (a), emitted photon number $\bar{n}_\gamma$ (b), and $\bar{\chi}_e$ (c) averaged over electrons with $(\theta, \phi) \in [-20°, 20°]$: for final momentum $p_x^f > 0$ (blue solid line) and $p_x^f < 0$ (red dashed line).

2. Large angle electrons: Polarization along the electric field

The spin precession also plays a role in electron spin dynamics, leading to rotation of the polarization vector along velocity direction with a frequency

$$\frac{d\zeta_x(\varphi)}{d\varphi} = -\omega_s(\varphi)\zeta_y(\varphi)$$
$$\omega_s(\varphi) \approx \frac{|e|\gamma}{mk\cdot p}\left[\left(\frac{g}{2}-1\right)\left(1-\frac{\gamma}{\gamma+1}v_z\right)+\frac{1}{\gamma+1}\right]v_y E_x(\varphi). \tag{4}$$

Before the arrival of the laser pulse peak, the spin precession is insignificant due to the smallness of v_y, while becoming notable near the pulse peak, especially for electrons moving at large (θ, ϕ), due to the enhancement of ponderomotive force associated with finite beam size. Take the electrons within $\theta > 0$ and $\varphi > 20°$ for an example, see Fig. 6. These electrons are initially distributed with $\bar{y}(0) > 0$ and move in the x–z plane before they meet the laser peak at $\varphi/2\pi = 4.55$ [Fig. 6(c)]. When the laser peak arrives, the electrons are accelerated to $p_y > 0$ because of the ponderomotive force $F_y \propto y > 0$. Consequently, the spin precession starts to take effect inducing a transverse polarization along the electric field ζ_x via Eq. (4) [Fig. 6(d)], while the spin

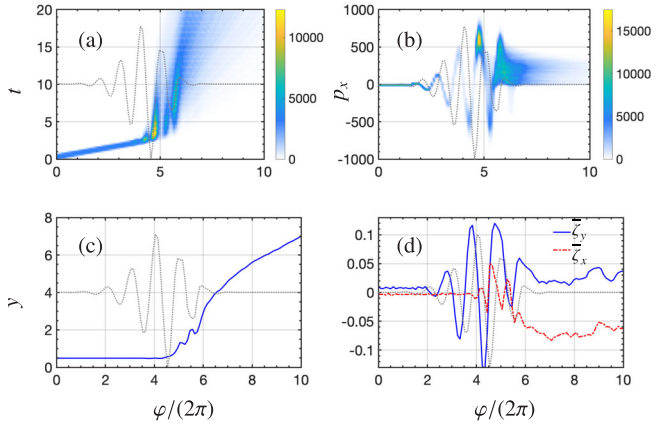

FIG. 6. (a) The number density $d^2N/(dtd\varphi)$ vs evolution time t/T and phase $\varphi/2\pi$. (b) The number density $d^2N/(dp_x d\varphi)$ vs p_x and $\varphi/2\pi$. (c) The evolution of y/λ_0 vs laser phase $\varphi/2\pi$. (d) Average polarization $\bar{\zeta}_x$ (blue solid line) and $\bar{\zeta}_y$ (red dashed line) vs laser phase $\varphi/2\pi$. The electrons are within $\theta > 20°$ and $\phi > 20°$. The superimposed dot-dashed lines in (a) and (b) are the corresponding magnetic fields.

dynamics of ζ_y are still determined by radiative polarization until the electrons run away from the beam center after $\varphi/2\pi \approx 5.55$ [Figs. 6(a) and 6(b)]. Assuming the electrons move in a monochromatic plane wave $E(\varphi) = E_0 \cos\varphi$, the radiative polarization gives rise to a transverse polarization $\zeta_y \propto -\sin\varphi$, while the spin precession induces a rotation of the spin to $\zeta_x \propto -\cos(2\varphi)/4$, which qualitatively is in accordance with the spin dynamics shown in Fig. 6(d). As electrons are escaping the laser beam at the negative half-cycle peaked at $\varphi/2\pi = 5.55$, they gain positive ζ_y and negative ζ_x, as shown in Figs. 2(a) and 2(b). In contrast, the electrons with small ϕ are free from spin precession even after the main peak arrives since the ponderomotive force along y ($F_y \propto y$) is negligible along the x-axis ($\varphi = 0°$). Therefore, the electrons distributed at $\varphi \sim 0$ have negligible ζ_x and a maximum for ζ_y, see Figs. 2(a) and 2(b).

3. Small angle electrons: Angle-dependent polarization

Now let us discuss the polarization of the electrons in a small angle region. At $t = 20T$, the reflected electrons could either be scattered out of the laser beam in the transverse direction or still propagate forward along with the laser beam. The former corresponds to the case of the large-angle electrons described above, while the latter to the small-angle electrons which have opposite polarization (see Fig. 2). To analyze polarization features in the small angle region, we select the electrons with final polar angle within $[-10°, 10°]$ and plot their trajectory, as well as the evolution of momentum, see Fig. 7. Apparently, the small-angle electrons are initially distributed around the beam center with $\bar{x}(0) \sim 0$, see Fig. 7 (Top row). Unlike the off-axis electrons, the on-axis electrons are less likely to be scattered out

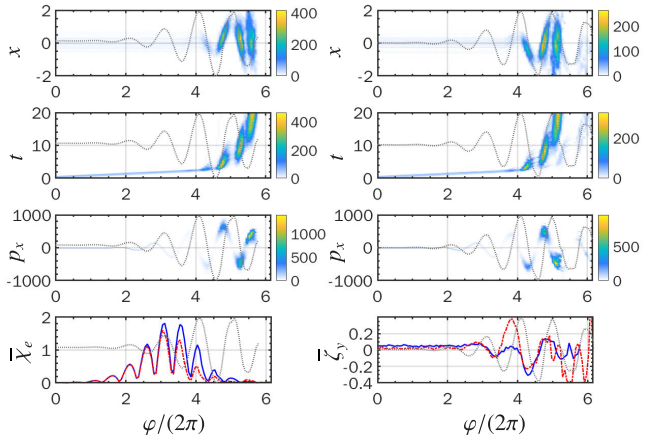

FIG. 7. (Top row) The trajectory x, (second row) evolution time t, and (third row) momentum evolution p_x vs the laser phase $\varphi/2\pi$, for electrons within $\theta \in [-10°, 10°]$ and $\phi \in [-20°, 20°]$; for electrons with final momentum $p_x^f > 0$ (left column), and $p_x^f < 0$ (right column); (last row) $\bar{\chi}_e$ and $\bar{\zeta}_y$ vs the laser phase $\varphi/2\pi$ for electrons with final momentum $p_x^f > 0$ (blue solid line) and $p_x^f < 0$ (red dashed line).

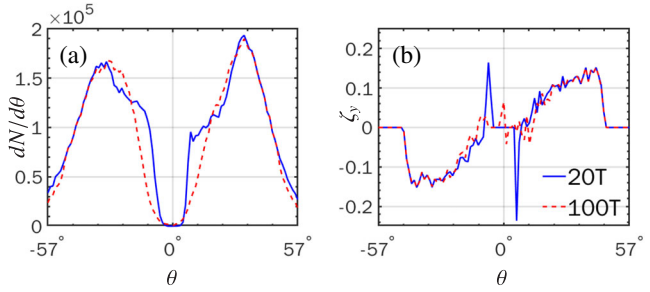

FIG. 8. The particle number distribution $dN/d\theta$ (a) and the averaged spin component ζ_y (b) at $t = 20T$ (solid blue line) and $t = 100T$ (dash red line).

of the beam when the laser peak arrives. When the on-axis electrons meet the negative half-cycle peaked at $\varphi/2\pi = 4.55$, they are accelerated to relativistic velocity and stay in the half-cycle $4.55 < \varphi/2\pi < 5.05$ for a few periods [see Fig. 7 (second row)], during which the electrons move towards $x > 0$ with $p_x > 0$ [see Fig. 7 (third row)]. The radiative polarization still is non-negligible at this point as $\chi_e \sim 0.45$ and induces polarization $\zeta_y > 0$ correlated with momentum $p_x > 0$. Unlike the large-angle electrons, the small-angle electrons are not scattered off the laser beam but continue to oscillate inside the laser beam. In the next half-cycle, the momentum p_x becomes negative, but the polarization ζ_y could not keep up with the changes of p_x as the radiative polarization is gradually suppressed along with decreasing χ_e, see Fig. 7 (fourth row). For instance, at the detection time $t = 20T$, the electrons with $p_x^f < 0$ are centred at $\varphi/2\pi = 5.156$; they have $p_x < 0$ [Fig. 7] but still $\zeta_y > 0$ [Fig. 7]. Therefore, after reflection, the polarization of the small-angle electrons is barely changed as $\chi_e \to 0$ while the momentum p_x further evolves with laser fields, which breaks the correlation between p_x and ζ_y. At $t = 20T$, the dephasing between p_x and ζ_y causes the opposite polarization for electrons distributed at small and large angles. However, the angle-dependent polarization observed at $t = 20T$ is not stable for small angle electrons since p_x further evolves with time as long as the electrons stay in the laser field. The electrons with different polarization could be mixed with each other, leading to a vanishing polarization for small angle electrons at $t = 100T$. In contrast, the electrons in a large angle region are free from depolarization as they are already out of laser pulse at $t = 20T$ (see Fig. 8).

B. Polarization of created pairs

The strong interaction induces efficient pair production; the number of emitted pairs per laser cycle is [42]

$$N_{e+e-} \approx N_\gamma \frac{27\Gamma^7(2/3)\alpha m\lambda}{56\pi^5\omega_\gamma\lambda_C}\left(\frac{3\chi_\gamma}{2}\right)^{2/3}. \quad (5)$$

When each electron during a single laser cycle emits one high energy photon, $N_\gamma \sim \alpha a_0 \sim 1$; for our parameters

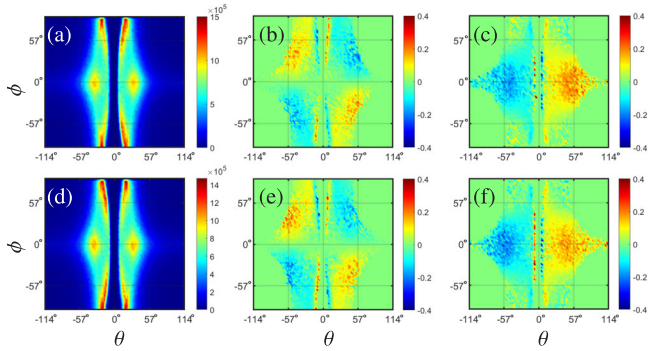

FIG. 9. Angular distribution $d^2N/d\Omega$ vs the polar angle θ (degree) and the azimuthal angle ϕ (degree): (a) for produced electrons e^- and (d) for positrons e^+. The averaged polarization distribution along the electric field direction ζ_x: (b) for e^- and (e) for e^+. The averaged polarization distribution along the magnetic field direction ζ_y: (c) for e^- and (f) for e^+.

one can achieve $N_{e+e-} \sim 1$ per laser cycle via Eq. (5). In qualitative terms this means that each electron emits one high-energy photon, which further is converted to an electron-positron pair in one laser cycle, yielding one positron per each initial electron. In this case, the positron number is comparable with the number of seed electrons (this yield is about 2 orders of magnitude larger than that of Ref. [50] using a two-color scheme).

Similar to the seed electrons, the created pairs are polarized with $\zeta_y > 0$ at $\theta > 0$ and $\zeta_y < 0$ at $\theta < 0$, but with more particles distributed at $\theta > 20°$ (see Fig. 9). This is because the created pairs have a larger $\bar{x}_{\pm}(0)$ than that of initial electrons and therefore more likely to be scattered out of the laser beam than captured by it. The polarization mechanism for seed electrons also works for the produced pairs. The created electrons and positrons are polarized according to the quantization axis in the creation phase. Positron (electron) polarization is most probably to be along (opposite to) the laser magnetic field. Therefore, the positrons (electrons) created at $B_y > 0$ are likely to be polarized with $\zeta_y^+ > 0$ ($\zeta_y^- < 0$). After creation, these positrons (electrons) with $\zeta_y^+ > 0$ ($\zeta_y^- < 0$) lost most of their energy due to significant radiation at the half-cycle $B_y > 0$ since the radiation probability dW_{ζ_i,ζ_f} for positrons (electrons) is dominated by $dW_{\uparrow,\uparrow}$ ($dW_{\downarrow,\downarrow}$). The reflected positrons (electrons) are rapidly accelerated to relativistic velocity and stay at the acceleration phase $B_y > 0$, $p_x^+ > 0$ ($B_y > 0$, $p_x^- < 0$) for a long time, during which the positrons (electrons) with $x(0)^+ > 0$ ($x(0)^- < 0$) can be rapidly scattered out of the laser beam (Fig. 10). Consequently, the positrons (electrons) created at $B_y > 0$, $\zeta_y^+ > 0$ ($\zeta_y^- < 0$) have final momentum $p_x^f > 0$ ($p_x^f < 0$), while created at $B_y < 0$, $\zeta_y^+ < 0$ ($\zeta_y^- > 0$) have $p_x^f < 0$ ($p_x^f > 0$). Therefore, the angle distribution of density and polarization for pairs are similar to seed electrons, except for a higher density distribution in the large angle region.

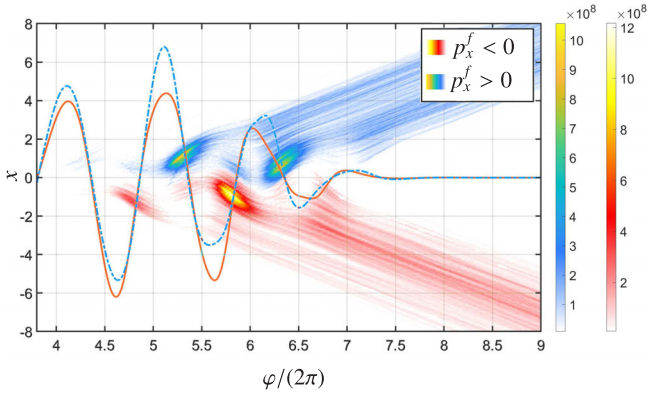

FIG. 10. The trajectory x of positrons within $|\theta| \in [50°, 60°]$ and $\phi \in [-20°, 20°]$ vs the laser phase φ for positrons with $p_x^f > 0$ (parula) and $p_x^f < 0$ (hot). The superimposed lines are the corresponding magnetic fields.

IV. IMPACT OF LASER AND ELECTRON PARAMETERS

For experimental convenience, we investigate the impact of laser and electron parameters on polarization, see Fig. 11. The average polarization $\bar{\zeta}_y$ is inversely proportional to the seed electrons energy [Fig. 11(a)]. This is because the energetic electrons can penetrate through the laser pulse instead of being reflected. Since the forward electrons have vanishing average polarization in a symmetric laser field, the average polarization decreases with higher electron energy. The dependence of $\bar{\zeta}_y$ on ε_0 is less sensitive for larger a_0 since the radiation loss is more dramatic in an intense laser field, which is beneficial for the occurrence of reflection and suppresses forward scattering. Meanwhile, an intense laser pulse provides a higher transverse acceleration and stronger focusing effects, making it easier for electrons to escape the field with correlated polarization and deflection angle. Therefore, with the increase of a_0 the average polarization increases. To show the importance of the focusing effect, we simulate the

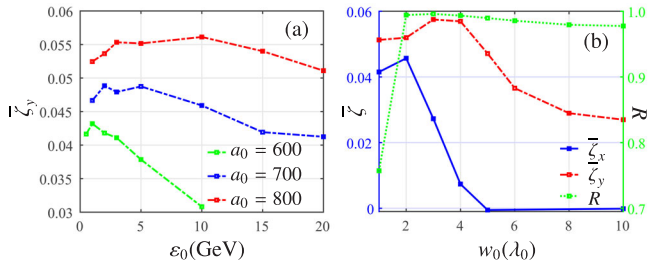

FIG. 11. (a) The average polarization $\bar{\zeta}_y$ for electrons with $\theta > 0$ vs seed electron energy ε_0 for $a_0 = 600$ (blue solid), $a_0 = 700$ (red dashed), and $a_0 = 800$ (green dotted), respectively. (b) The average polarization $\bar{\zeta}_x$ at $\theta < 0$, $\phi > 0$ (blue-solid), $\bar{\zeta}_y$ at $\theta > 0$ (red dashed) and reflectivity R of the electron beam vs laser beam waist w_0, $a_0 = 760$.

scattering with various laser beam waists w_0. Generally, the average polarization decreases with the increase of the beam waist due to the weaker focusing effects at larger w_0 [Fig. 11(b)]. However, $\bar{\zeta}_y$ increases with the growth of w_0 at $w_0 \leq 3\lambda_0$, which can be explained as follows. As is shown in Sec. III A 2, the ponderomotive force in a tightly focused laser beam induces a rotation of the polarization vector. When the beam waist decreases from $3\lambda_0$ to $2\lambda_0$, the enhanced ponderomotive force causes the decrease of $\bar{\zeta}_y$ and increase of $\bar{\zeta}_x$ [Fig. 11(b)]. Meanwhile, when the laser beam waist is further decreased, part of the electron beam may not be able to interact with strong lasers and consequently cannot be reflected. The reflection rate decreases to 76% at $w_0 = \lambda_0$, resulting in a decrease of $\bar{\zeta}_x$ and $\bar{\zeta}_y$ [Fig. 11(b)]. Therefore, $\bar{\zeta}_y$ increases with w_0 at $w_0 \leq 3\lambda_0$ as a result of enhanced spin precession and a reduction in the reflection rate.

The impact of initial transverse displacement of the electron beam is analyzed in Fig. 12. For $\Delta\bar{x}(0) = \lambda_0/2$, the symmetric angular distribution of electrons is distorted, with more electrons moving towards $\theta > 0$ and $\zeta_y > 0$, see Fig. 12. The electrons with larger initial displacement are more likely to be scattered out of laser field, and consequently more electrons are distributed in the larger angle region [Figs. 12(a) and 12(c)], where the polarization degree is higher [Figs. 12(b) and 12(d)]. Therefore, a finite displacement of the electron beam from the laser pulse axis is beneficial for polarization. However, $\Delta\bar{x}(0)$ should be restricted, because the electrons far away from the laser beam axis would experience a rather weak field, which will reduce the average polarization of the beam.

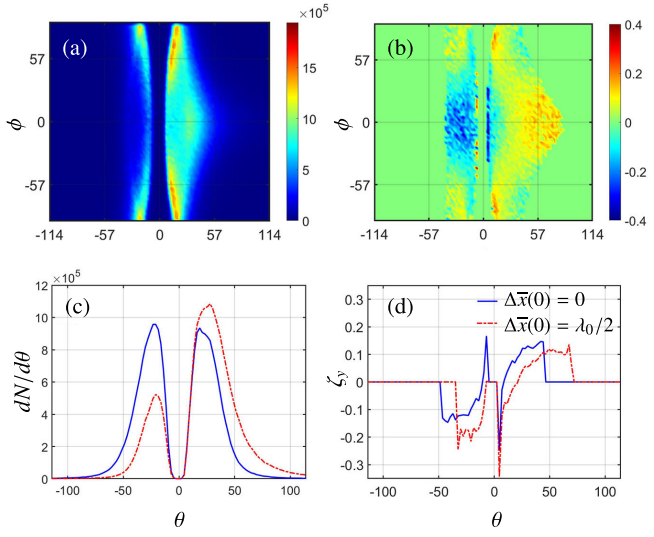

FIG. 12. Angular distribution of $d^2N/d\Omega$ (a) and averaged polarization distribution along the magnetic field direction ζ_y (b) versus the polar angle θ (degree) and the azimuthal angle ϕ (degree) for electrons with an initial displacement of $\Delta\bar{x}(0) = \lambda_0/2$. The electron number distribution $dN/d\theta$ (c) and the averaged spin component ζ_y (d) versus polar angle θ for electron beam with (solid blue line) and without (dash red line) initial beam displacement.

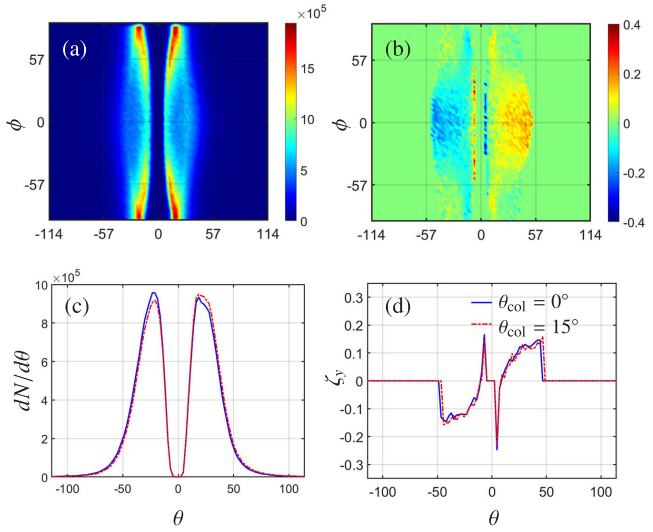

FIG. 13. Angular distribution of $d^2N/d\Omega$ (a) and averaged polarization distribution along the magnetic field direction ζ_y (b) versus the polar angle θ (degree) and the azimuthal angle ϕ (degree) for electrons with a collision angle $\theta_{col} = 15°$ and displacement $\Delta\bar{x}(0) = -\lambda_0/2$. The electron number distribution $dN/d\theta$ (c) and the averaged spin component ζ_y (d) versus polar angle θ for electron beam with $\theta_{col} = 0°$ (solid blue line) and $\theta_{col} = 15°$ (dash red line).

Finally, we have investigated the impact of the collision angle between laser pulse and electron beam axis, see Fig. 13. We rotate the electron beam clockwise in the x–z plane around the beam center with $\theta_{col} = 15°$ and shift the beam downwards with a displacement of $\Delta\bar{x}(0) = -\lambda_0/2$ for a collision. As discussed above, the negative displacement causes more electrons to be deflected towards $\theta < 0$ and $\zeta_y < 0$. However, some particles starting with negative displacement along the x axis can enter the region of positive displacement due to the initial momentum. The initial momentum cancels out the polarization effects of displacement, leading to a negligible variation of angular distribution [Figs. 13(c) and 13(d)]. Therefore, our results are robust with regard to the collision angle.

V. CONCLUSION

We have demonstrated that an electron beam counterpropagating an ultrastrong ultrashort laser pulse can be polarized in the QRDR due to reflections. With a similar mechanism the crated electron-positron pairs during the interaction are polarized, resulting in the generation of a dense beam of polarized particles with a linearly polarized laser pulse. Strong spin-dependent radiation reaction is essential to enable the reflection scenario and creates angle-dependent polarization in tightly focused laser fields.

The tightly focusing of the laser beam and its ultrashort duration are necessary ingredients to enable the polarization mechanism. After the interaction of reflected particles with the dominant half-cycle, the field intensity is dramatically decreased due to the focusing effect of the laser field, resulting in the asymmetric and correlated kinetic and spin dynamics. Particles distributed with large transverse position can be scattered out of the laser beam rapidly within the acceleration cycle, leading to the angle-dependent polarization along the laser magnetic field.

Furthermore, we have found that the spin precession also plays a role for developing polarization features of the reflected particles. It reduces the polarization degree along the magnetic field induced by the radiative polarization, diverting it to the angle-dependent polarization along the electric field. In the same setup efficient pair production and their polarization with the same mechanism takes place. For instance, with a possible ultrahigh-charge ($\sim$100 nC) electron beam, a polarized positron beam with a density of 10^9–10^{10}/bunch is foreseeable.

The important point of the presented reflection scheme of the particle polarization is that the polarization arises from the asymmetric laser-electron interaction dynamics, and it does not demand the challenging task of constructing asymmetric strong laser fields. With next generation laser facilities, the reflection scheme may provide a relatively simple way of producing dense polarized lepton beams and a valuable tool to search for qualitative signatures of radiative spin effects.

ACKNOWLEDGMENTS

This work has been supported by the National Natural Science Foundation of China (Grants No. 12074262 and No. 12222507), the National Key R&D Program of China (2021YFA1601700), the Shanghai Rising-Star Program, and the Shanghai Natural Science Foundation (Grant No. 20ZR1441600).

APPENDIX A: SPIN- AND POLARIZATION-RESOLVED MONTE CARLO METHOD FOR NONLINEAR COMPTON SCATTERING

In this section, we summarize the spin- and polarization-resolved Monte Carlo method for nonlinear Compton scattering, which was developed in our previous works [47–49,55,63] (also see [54] for a similar algorithm).

1. Spin- and polarization-resolved photon emission probability

The radiation probability including all the polarization and spin characteristics takes the form

$$dW^R(\boldsymbol{\zeta},\boldsymbol{\zeta}',\boldsymbol{\xi}) = \frac{1}{2}(F_0 + \xi_1 F_1 + \xi_2 F_2 + \xi_3 F_3), \quad \text{(A1)}$$

where the three-vector $\boldsymbol{\xi} = (\xi_1, \xi_2, \xi_3)$ is the Stokes parameter of the emitted photon, $F_0 = dW_{11} + dW_{22}$, $F_1 = dW_{12} + dW_{21}$, $F_2 = i(dW_{12} - dW_{21})$, $F_3 = dW_{11} - dW_{22}$, with the polarization matrix of radiation probability per unit time:

$$\begin{aligned}
dW_{11} + dW_{22} &= \frac{C_0}{2} d\omega \left\{ \left[\frac{\varepsilon^2 + \varepsilon'^2}{\varepsilon'\varepsilon} \mathrm{K}_{\frac{2}{3}}(z_q) - \int_{z_q}^{\infty} dx \mathrm{K}_{\frac{1}{3}}(x) \right] + \left[2\mathrm{K}_{\frac{2}{3}}(z_q) - \int_{z_q}^{\infty} dx \mathrm{K}_{\frac{1}{3}}(x) \right] \boldsymbol{\zeta}\cdot\boldsymbol{\zeta}' - \left[\frac{\omega}{\varepsilon} \boldsymbol{\zeta}\cdot\mathbf{b} + \frac{\omega}{\varepsilon'} \boldsymbol{\zeta}'\cdot\mathbf{b} \right] \mathrm{K}_{\frac{1}{3}}(z_q) \right. \\
&\quad \left. + \frac{\omega^2}{\varepsilon'\varepsilon} \left[\mathrm{K}_{\frac{2}{3}}(z_q) - \int_{z_q}^{\infty} dx \mathrm{K}_{\frac{1}{3}}(x) \right] (\boldsymbol{\zeta}\cdot\hat{\mathbf{v}})(\boldsymbol{\zeta}'\cdot\hat{\mathbf{v}}) \right\}, \\
dW_{12} + dW_{21} &= \frac{C_0}{2} d\omega \left\{ \frac{\varepsilon^2 - \varepsilon'^2}{2\varepsilon'\varepsilon} \mathrm{K}_{\frac{2}{3}}(z_q) (\hat{\mathbf{v}}[\boldsymbol{\zeta}'\times\boldsymbol{\zeta}]) + \left[\frac{\omega}{\varepsilon'} (\boldsymbol{\zeta}\cdot\mathbf{s}) + \frac{\omega}{\varepsilon} (\boldsymbol{\zeta}'\cdot\mathbf{s}) \right] \mathrm{K}_{\frac{1}{3}}(z_q) - \frac{\omega^2}{2\varepsilon'\varepsilon} \int_{z_q}^{\infty} dx \mathrm{K}_{\frac{1}{3}}(x) [(\boldsymbol{\zeta}\cdot\mathbf{s})(\boldsymbol{\zeta}'\cdot\mathbf{b}) \right. \\
&\quad \left. + (\boldsymbol{\zeta}\cdot\mathbf{b})(\boldsymbol{\zeta}'\cdot\mathbf{s})] \right\}, \\
dW_{12} - dW_{21} &= i\frac{C_0}{2} d\omega \left\{ \frac{\varepsilon^2 - \varepsilon'^2}{2\varepsilon'\varepsilon} \mathrm{K}_{\frac{1}{3}}(z_q) (\mathbf{s}\cdot[\boldsymbol{\zeta}'\times\boldsymbol{\zeta}]) + \left(-\frac{\varepsilon^2 - \varepsilon'^2}{\varepsilon'\varepsilon} \mathrm{K}_{\frac{2}{3}}(z_q) + \frac{\omega}{\varepsilon} \int_{z_q}^{\infty} dx \mathrm{K}_{\frac{1}{3}}(x) \right) (\boldsymbol{\zeta}\cdot\hat{\mathbf{v}}) \right. \\
&\quad \left. + \left(-\frac{\varepsilon^2 - \varepsilon'^2}{\varepsilon'\varepsilon} \mathrm{K}_{\frac{2}{3}}(z_q) + \frac{\omega}{\varepsilon'} \int_{z_q}^{\infty} dx \mathrm{K}_{\frac{1}{3}}(x) \right) (\boldsymbol{\zeta}'\cdot\hat{\mathbf{v}}) + \frac{\omega^2}{2\varepsilon'\varepsilon} \mathrm{K}_{\frac{1}{3}}(z_q) [(\boldsymbol{\zeta}\cdot\hat{\mathbf{v}})(\boldsymbol{\zeta}'\cdot\mathbf{b}) + (\boldsymbol{\zeta}\cdot\mathbf{b})(\boldsymbol{\zeta}'\cdot\hat{\mathbf{v}})] \right\}, \\
dW_{11} - dW_{22} &= \frac{C_0}{2} d\omega \left\{ \mathrm{K}_{\frac{2}{3}}(z_q) + \frac{\varepsilon^2 + \varepsilon'^2}{2\varepsilon'\varepsilon} \mathrm{K}_{\frac{2}{3}}(z_q) \boldsymbol{\zeta}\cdot\boldsymbol{\zeta}' - \left[\frac{\omega}{\varepsilon'} (\boldsymbol{\zeta}\cdot\mathbf{b}) + \frac{\omega}{\varepsilon} (\boldsymbol{\zeta}'\cdot\mathbf{b}) \right] \mathrm{K}_{\frac{1}{3}}(z_q) \right. \\
&\quad \left. + \frac{\omega^2}{2\varepsilon'\varepsilon} \left(-\mathrm{K}_{\frac{2}{3}}(z_q) (\boldsymbol{\zeta}\cdot\hat{\mathbf{v}})(\boldsymbol{\zeta}'\cdot\hat{\mathbf{v}}) + \int_{z_q}^{\infty} dx \mathrm{K}_{\frac{1}{3}}(x) [(\boldsymbol{\zeta}\cdot\mathbf{b})(\boldsymbol{\zeta}'\cdot\mathbf{b}) - (\boldsymbol{\zeta}\cdot\mathbf{s})(\boldsymbol{\zeta}'\cdot\mathbf{s})] \right) \right\}, \quad \text{(A2)}
\end{aligned}$$

where $\boldsymbol{\zeta}$ and $\boldsymbol{\zeta}'$ are the spin polarization vectors before and after emission, ε and ε' the corresponding electron energies, $z_q = \frac{2}{3\chi_e}\frac{\omega}{\varepsilon'}$ with χ_e controlling the magnitude of quantum effects, $C_0 = \frac{\alpha}{\sqrt{3}\pi\gamma^2}$ and $\mathbf{b} = \hat{\mathbf{v}} \times \boldsymbol{s}$ with $\hat{\mathbf{v}}$ and $\boldsymbol{s}$ being unit vectors along the direction of electron velocity and acceleration, respectively.

a. Spin quantization axis for final electron spin

After summing over the polarization of emitted photons, we obtain the probability for emitting a photon with an energy ω and spin $\boldsymbol{\zeta}'$ during the time step Δt:

$$
\begin{aligned}
d\bar{W}^R(\boldsymbol{\zeta},\boldsymbol{\zeta}') &= \frac{1}{2}(a + \boldsymbol{b}\cdot\boldsymbol{\zeta}') \\
a &= C_0 d\omega \left\{ \frac{\varepsilon^2+\varepsilon'^2}{\varepsilon'\varepsilon} \mathrm{K}_{\frac{2}{3}}(z_q) - \int_{z_q}^{\infty} dx \mathrm{K}_{\frac{1}{3}}(x) - \frac{\omega}{\varepsilon}\boldsymbol{\zeta}\mathbf{b}\mathrm{K}_{\frac{1}{3}}(z_q) \right\}, \\
\boldsymbol{b} &= C_0 d\omega \left\{ \left[2\mathrm{K}_{\frac{2}{3}}(z_q) - \int_{z_q}^{\infty} dx \mathrm{K}_{\frac{1}{3}}(x) \right] \boldsymbol{\zeta} - \frac{\omega}{\varepsilon'}\mathrm{K}_{\frac{1}{3}}(z_q)\mathbf{b} + \frac{\omega^2}{\varepsilon'\varepsilon} \left[\mathrm{K}_{\frac{2}{3}}(z_q) - \int_{z_q}^{\infty} dx \mathrm{K}_{\frac{1}{3}}(x) \right] (\boldsymbol{\zeta}\cdot\hat{\mathbf{v}})\hat{\mathbf{v}} \right\}.
\end{aligned} \tag{A3}
$$

The final polarization vector of the electron resulting from the scattering process itself is $\boldsymbol{\zeta}_f^R = \frac{\boldsymbol{b}}{a}$, which determines the spin quantization axis for electrons after radiation adopted in our Monte Carlo simulations: $\boldsymbol{n}^R = \boldsymbol{\zeta}_f^R/|\boldsymbol{\zeta}_f^R|$.

b. Polarization quantization axis for emitted photon

Summing over the final electron polarizations, the radiation probability becomes

$$
\begin{aligned}
d\tilde{W}^R(\boldsymbol{\zeta},\boldsymbol{\xi}) &= \frac{1}{2}(\tilde{F}_0 + \xi_1\tilde{F}_1 + \xi_2\tilde{F}_2 + \xi_3\tilde{F}_3), \\
\tilde{F}_0 &= C_0 d\omega \left\{ \frac{\varepsilon^2+\varepsilon'^2}{\varepsilon'\varepsilon} \mathrm{K}_{\frac{2}{3}}(z_q) - \int_{z_q}^{\infty} dx \mathrm{K}_{\frac{1}{3}}(x) - \frac{\omega}{\varepsilon}\boldsymbol{\zeta}\cdot\mathbf{b}\mathrm{K}_{\frac{1}{3}}(z_q) \right\}, \\
\tilde{F}_1 &= C_0 d\omega \frac{\omega}{\varepsilon'}(\boldsymbol{\zeta}\cdot\mathbf{s})\mathrm{K}_{\frac{1}{3}}(z_q), \\
\tilde{F}_2 &= -C_0 d\omega \left(-\frac{\varepsilon^2-\varepsilon'^2}{\varepsilon'\varepsilon}\mathrm{K}_{\frac{2}{3}}(z_q) + \frac{\omega}{\varepsilon}\int_{z_q}^{\infty} dx \mathrm{K}_{\frac{1}{3}}(x) \right)(\boldsymbol{\zeta}\cdot\hat{\mathbf{v}}), \\
\tilde{F}_3 &= C_0 d\omega \left\{ \mathrm{K}_{\frac{2}{3}}(z_q) - \frac{\omega}{\varepsilon'}(\boldsymbol{\zeta}\cdot\mathbf{b})\mathrm{K}_{\frac{1}{3}}(z_q) \right\}.
\end{aligned} \tag{A4}
$$

The polarization of the emitted photon resulting from the scattering process itself takes the form $\boldsymbol{\xi}_f = (\tilde{F}_1/\tilde{F}_0, \tilde{F}_2/\tilde{F}_0, \tilde{F}_3/\tilde{F}_0)$, which determines the quantization axis for the emitted photons' polarization: $\boldsymbol{n}_\gamma^R = \boldsymbol{\xi}_f/|\boldsymbol{\xi}_f|$.

After summing over final polarizations, we obtain the spectral probability depending on the initial spin of the electron $\boldsymbol{\zeta}$:

$$
dW_T^R(\boldsymbol{\zeta}) = \tilde{F}_0. \tag{A5}
$$

2. Spin-resolved no-emission probability

While electron polarization emerges mostly due to spin-flips at photon emissions, there is a nonradiative contribution to the polarization which stems from the one-loop QED radiative corrections to the self-energy. In physical terms, the nonradiative polarization effect emerges due to the dependence of the photon emission probability on the initial electron spin. The electrons which do not emit will be polarized because the emission is preferred in a certain spin state. For a detailed discussions on this topic, please refer to our recent paper [66].

The spin-resolved no-emission probability can be derived from the emission probability Eq. (A5) based on unitarity:

$$W^{NR}(\boldsymbol{\zeta},\boldsymbol{\zeta}') = \frac{1}{2}(c + \boldsymbol{\zeta}'\cdot\boldsymbol{d}),$$
$$c = 1 - \int_0^{\varepsilon} \tilde{F}_0 d\omega\Delta t,$$
$$\boldsymbol{d} = \boldsymbol{\zeta}\left(1 - \int_0^{\varepsilon} \bar{F}_0 d\omega\Delta t\right) + \mathbf{b}C_0 \int_0^{\varepsilon} \frac{\omega}{\varepsilon} \mathrm{K}_{\frac{1}{3}}(z_q) d\omega\Delta t, \quad \text{(A6)}$$

where

$$\bar{F}_0 = C_0 d\omega \left\{ \frac{\varepsilon^2 + \varepsilon'^2}{\varepsilon'\varepsilon} \mathrm{K}_{\frac{2}{3}}(z_q) - \int_{z_q}^{\infty} dx \mathrm{K}_{\frac{1}{3}}(x) \right\}.$$

The final polarization vector of the electron resulting from the scattering process itself is $\boldsymbol{\zeta}_f^{NR} = \frac{\boldsymbol{d}}{c}$, which determines the spin quantization axis for electrons after no-emission process: $\boldsymbol{n}^{NR} = \boldsymbol{\zeta}_f^{NR}/|\boldsymbol{\zeta}_f^{NR}|$.

3. Classical spin precession in the external laser field

Between quantum events, the electron dynamics in the ultraintense laser field is described by the Lorenz equation

$$d\mathbf{p}/dt = e(\mathbf{E} + \boldsymbol{\beta}\times\mathbf{B}). \quad \text{(A7)}$$

The spin procession is governed by the Thomas-Bargmann-Michel-Telegdi equation:

$$\frac{d\mathbf{S}}{dt} = \frac{e}{m}\mathbf{S}\times\left[-\left(\frac{g}{2}-1\right)\frac{\gamma}{\gamma+1}(\boldsymbol{\beta}\cdot\mathbf{B})\boldsymbol{\beta} + \left(\frac{g}{2}-1+\frac{1}{\gamma}\right)\mathbf{B} - \left(\frac{g}{2}-\frac{\gamma}{\gamma+1}\right)\boldsymbol{\beta}\times\mathbf{E}\right], \quad \text{(A8)}$$

where $\mathbf{E}$ and $\mathbf{B}$ are the laser electric and magnetic fields, respectively, and g is the electron gyromagnetic factor: $g(\chi_e) = 2 + 2\mu(\chi_e)$, $\mu(\chi_e) = \frac{\alpha}{\pi\chi_e}\int_0^{\infty}\frac{y}{(1+y)^3}\mathbf{L}_{\frac{1}{3}}(\frac{2y}{3\chi_e})dy$, with $\mathbf{L}_{\frac{1}{3}}(z) = \int_0^{\infty}\sin[\frac{3z}{2}(x+\frac{x^3}{3})]dx$. As $\chi_e \ll 1$, $g \approx 2.00232$.

4. Algorithm of event generation

a. Decide photon emission event

At each simulation step, the photon emission and the photon energy are determined by the spectral probability dW_T^R of Eq. (A5), using the common stochastic procedure:

(1) Generate two random numbers $r_1, r_2 \in [0,1]$ with uniform probability.

(2) Compute the radiation probability $P_m(r_1)$ for the given initial spin $\boldsymbol{\zeta}$ and photon energy $\omega = r_1^3\varepsilon$. The probability $P_m(r_1)$ in a given time interval Δt is computed using [68]

$$P_m(r_1) = \frac{\partial f(r_1)}{\partial r_1} P[f(r_1)], \quad \text{(A9)}$$

with $f(x) = x^3$ and $P(\omega) = dW_T^R(\boldsymbol{\zeta},\omega)\Delta t$, i.e. $P(r_1) = 3r_1^2 dW_T^R(\boldsymbol{\zeta}, r_1^3\varepsilon)\Delta t$ with $\Delta t = 10^{-3}T$.

(3) If $r_2 < P_m(r_1)$, then a photon is emitted with energy $\omega = r_1^3\varepsilon$. Otherwise, a photon emission is rejected.

b. Decide the polarization of outgoing particles

Case 1: $P_m(r_1) > r_2$: photon emission occurs. After each photon emission, the spin of the emitting particle (polarization of emitted photon) is either parallel or antiparallel to $\boldsymbol{n}^R$ ($\boldsymbol{n}_\gamma$) using the stochastic procedure with another random number $r_3 \in [0,1]$. For the given photon energy ω and initial spin $\boldsymbol{\zeta}$, compute the radiation probability $P_{\zeta'\xi} = dW^R(\boldsymbol{\zeta},\boldsymbol{\zeta}',\boldsymbol{\xi})\Delta t$. Here $\{\boldsymbol{\zeta}',\boldsymbol{\xi}\} \in \{\uparrow,\downarrow\}$ indicates the final spin is parallel or antiparallel with respect to the quantization axis.

(1) If $r_3 < P_{\downarrow\downarrow}$, then the electron is spin down with respect to $\boldsymbol{n}^R$, and the emitted photon is in the polarization state of $-\boldsymbol{n}_\gamma$.

(2) If $P_{\downarrow\downarrow} < r_3 < P_{\downarrow\downarrow} + P_{\downarrow\uparrow}$, then $\boldsymbol{\zeta}' = -\boldsymbol{n}^R$ and $\boldsymbol{\xi} = \boldsymbol{n}_\gamma$.

(3) If $P_{\downarrow\downarrow} + P_{\downarrow\uparrow} < r_3 < P_{\downarrow\downarrow} + P_{\downarrow\uparrow} + P_{\uparrow\downarrow}$, then $\boldsymbol{\zeta}' = \boldsymbol{n}^R$ and $\boldsymbol{\xi} = -\boldsymbol{n}_\gamma$.

(4) If $P_{\downarrow\downarrow} + P_{\downarrow\uparrow} + P_{\uparrow\downarrow} < r_3 < P_{\downarrow\downarrow} + P_{\downarrow\uparrow} + P_{\uparrow\downarrow} + P_{\uparrow\uparrow}$, then $\boldsymbol{\zeta}' = \boldsymbol{n}^R$ and $\boldsymbol{\xi} = \boldsymbol{n}_\gamma$.

Case 2: $P_m(r_1) < r_2$: photon emission is rejected. The electron spin state is collapsed into one of its basis states defined with respect to the instantaneous spin quantization axis $\boldsymbol{n}^{NR}$:

(1) Generate another random number $r_4 \in [0,1]$.

(2) Compute $P_{\zeta'} = W^{NR}(\boldsymbol{\zeta},\boldsymbol{\zeta}')$ with $\boldsymbol{\zeta}' \in \{\uparrow,\downarrow\}$ indicating spin parallel or antiparallel with $\boldsymbol{n}^{NR}$.

(3) If $P_\uparrow/(P_\uparrow + P_\downarrow) > r_4$, then $\boldsymbol{\zeta}' = \boldsymbol{n}^{NR}$; otherwise, $\boldsymbol{\zeta}' = -\boldsymbol{n}^{NR}$.

Note that, in our algorithm, the spin of the electron after the emission is determined by the spin-resolved emission probabilities according to the stochastic algorithm and instantaneously collapses into one of its basis states defined with respect to the instantaneous spin quantization axis (SQA). The pure state is more physically meaningful and more suitable to show a realistic detection result. Alternatively, one could set the final electron after emission in a mixed spin state $\boldsymbol{\zeta}' = \boldsymbol{\zeta}_f^R$ and photon polarization $\boldsymbol{\xi} = \boldsymbol{\xi}_f$; or $\boldsymbol{\zeta}' = \boldsymbol{\zeta}_f^{NR}$ in the case of no emission. The mixed state is more relevant for describing the average

polarization of electron ensembles or macroparticles in particle-in-cell. Nevertheless, these two methods are equivalent for sufficient running [69].

APPENDIX B: SPIN- AND POLARIZATION-RESOLVED MONTE CARLO METHOD FOR BREIT-WHEELER PROCESS

In this section, we summarize the spin- and polarization-resolved Monte Carlo method for the Breit-Wheeler process.

1. Spin- and polarization-resolved pair production probability

The pair production probability including all the polarization and spin characteristics takes the form

$$\begin{aligned} dW^P(\boldsymbol{\xi},\boldsymbol{\zeta}_-,\boldsymbol{\zeta}_+) &= \frac{1}{2}(dW_{11}+dW_{22}) + \frac{\xi_1}{2}(dW_{11}-dW_{22}) - i\frac{\xi_2}{2}(dW_{21}-dW_{12}) + \frac{\xi_3}{2}(dW_{11}-dW_{22}) \\ &= \frac{1}{2}(G_0+\xi_1 G_1+\xi_2 G_2+\xi_3 G_3), \end{aligned} \tag{B1}$$

where

$$\begin{aligned} G_0 &= \frac{\bar{C}_0}{2}d\varepsilon\Bigg\{\left\{\int_{z_p}^{\infty}dx\mathrm{K}_{\frac{1}{3}}(x)+\frac{\varepsilon_+^2+\varepsilon^2}{\varepsilon_+\varepsilon}\mathrm{K}_{\frac{2}{3}}(z_p)\right\}+\left\{\int_{z_p}^{\infty}dx\mathrm{K}_{\frac{1}{3}}(x)-2\mathrm{K}_{\frac{2}{3}}(z_p)\right\}(\boldsymbol{\zeta}_-\cdot\boldsymbol{\zeta}_+) \\ &\quad+\left[\frac{\omega}{\varepsilon_+}(\boldsymbol{\zeta}_+\cdot\mathbf{b})-\frac{\omega}{\varepsilon}(\boldsymbol{\zeta}_-\cdot\mathbf{b})\right]\mathrm{K}_{\frac{1}{3}}(z_p)+\left\{\frac{\varepsilon_+^2+\varepsilon^2}{\varepsilon\varepsilon_+}\int_{z_p}^{\infty}dx\mathrm{K}_{\frac{1}{3}}(x)-\frac{(\varepsilon_+-\varepsilon)^2}{\varepsilon\varepsilon_+}\mathrm{K}_{\frac{2}{3}}(z_p)\right\}(\boldsymbol{\zeta}_-\cdot\hat{\mathbf{v}})(\boldsymbol{\zeta}_+\cdot\hat{\mathbf{v}})\Bigg\} \\ G_1 &= \frac{\bar{C}_0}{2}d\varepsilon\Bigg\{-\frac{\varepsilon_+^2-\varepsilon^2}{2\varepsilon_+\varepsilon}\mathrm{K}_{\frac{2}{3}}(z_p)\hat{\mathbf{v}}\cdot(\boldsymbol{\zeta}_+\times\boldsymbol{\zeta}_-)+\left[\frac{\omega}{\varepsilon}(\boldsymbol{\zeta}_+\cdot\mathbf{s})-\frac{\omega}{\varepsilon_+}(\boldsymbol{\zeta}_-\cdot\mathbf{s})\right]\mathrm{K}_{\frac{1}{3}}(z_p) \\ &\quad-\frac{\omega^2}{2\varepsilon_+\varepsilon}\int_{z_p}^{\infty}dx\mathrm{K}_{\frac{1}{3}}(x)\{(\boldsymbol{\zeta}_-\cdot\mathbf{b})(\boldsymbol{\zeta}_+\cdot\mathbf{s})+(\boldsymbol{\zeta}_-\cdot\mathbf{s})(\boldsymbol{\zeta}_+\cdot\mathbf{b})\}\Bigg\} \\ G_2 &= \frac{\bar{C}_0}{2}d\varepsilon\Bigg\{-\frac{\omega^2}{2\varepsilon_+\varepsilon}\mathrm{K}_{\frac{1}{3}}(z_p)[\mathbf{s}\cdot(\boldsymbol{\zeta}_-\times\boldsymbol{\zeta}_+)]+\left(\frac{\omega}{\varepsilon_+}\int_{z_p}^{\infty}dx\mathrm{K}_{\frac{1}{3}}(x)+\frac{\varepsilon_+^2-\varepsilon^2}{\varepsilon_+\varepsilon}\mathrm{K}_{\frac{2}{3}}(z_p)\right)(\boldsymbol{\zeta}_+\cdot\hat{\mathbf{v}}) \\ &\quad+\left(\frac{\omega}{\varepsilon}\int_{z_p}^{\infty}dx\mathrm{K}_{\frac{1}{3}}(x)-\frac{\varepsilon_+^2-\varepsilon^2}{\varepsilon_+\varepsilon}\mathrm{K}_{\frac{2}{3}}(z_p)\right)(\boldsymbol{\zeta}_-\cdot\hat{\mathbf{v}})-\frac{\varepsilon_+^2-\varepsilon^2}{2\varepsilon_+\varepsilon}\mathrm{K}_{\frac{1}{3}}(z_p)[(\boldsymbol{\zeta}_-\cdot\hat{\mathbf{v}})(\boldsymbol{\zeta}_+\cdot\mathbf{b})+(\boldsymbol{\zeta}_-\cdot\mathbf{b})(\boldsymbol{\zeta}_+\cdot\hat{\mathbf{v}})]\Bigg\}, \\ G_3 &= \frac{\bar{C}_0}{2}d\varepsilon\Bigg\{-\mathrm{K}_{\frac{2}{3}}(z_p)+\frac{\varepsilon_+^2+\varepsilon^2}{2\varepsilon_+\varepsilon}\mathrm{K}_{\frac{2}{3}}(z_p)(\boldsymbol{\zeta}_-\cdot\boldsymbol{\zeta}_+)+\left[-\frac{\omega}{\varepsilon}(\boldsymbol{\zeta}_+\cdot\mathbf{b})+\frac{\omega}{\varepsilon_+}(\boldsymbol{\zeta}_-\cdot\mathbf{b})\right]\mathrm{K}_{\frac{1}{3}}(z_p) \\ &\quad-\frac{(\varepsilon_+-\varepsilon)^2}{2\varepsilon_+\varepsilon}\mathrm{K}_{\frac{2}{3}}(z_p)(\boldsymbol{\zeta}_-\cdot\hat{\mathbf{v}})(\boldsymbol{\zeta}_+\cdot\hat{\mathbf{v}})+\frac{\omega^2}{2\varepsilon_+\varepsilon}\int_{z_p}^{\infty}dx\mathrm{K}_{\frac{1}{3}}(x)[(\boldsymbol{\zeta}_-\cdot\mathbf{b})(\boldsymbol{\zeta}_+\cdot\mathbf{b})-(\boldsymbol{\zeta}_-\cdot\mathbf{s})(\boldsymbol{\zeta}_+\cdot\mathbf{s})]\Bigg\}. \end{aligned} \tag{B2}$$

Here $\bar{C}_0=\frac{\alpha m^2}{\sqrt{3}\pi\omega^2}$, $z_p=\frac{2}{3\chi_\gamma}\frac{\omega^2}{\varepsilon_+\varepsilon_-}$ and $\chi_\gamma=|F_{\mu\nu}k^\nu|/mF_{cr}$ controlling the magnitude of quantum effects, $\hat{\mathbf{v}}$ is the unit vector along velocity of the produced electron, $\mathbf{s}$ the unit vector along the transverse component of electron acceleration, and $\mathbf{b}=\hat{\mathbf{v}}\times\mathbf{s}$. The three-vector $\boldsymbol{\xi}=(\xi_1,\xi_2,\xi_3)$ is the Stokes parameter of the incoming photon, ω the photon energy, and ε_+ and ε_- are the energies of the created positron and electron, respectively.

a. Spin quantization axis for the produced electron

After taking the sum over positron polarizations,

$$
\begin{aligned}
d\tilde{W}^p(\boldsymbol{\xi},\boldsymbol{\zeta}_-) &= \frac{1}{2}(\tilde{G}_0+\xi_1\tilde{G}_1+\xi_2\tilde{G}_2+\xi_3\tilde{G}_3),\\
\tilde{G}_0 &= \bar{C}_0 d\varepsilon\left\{\int_{z_p}^{\infty} dx \mathrm{K}_{\frac{1}{3}}(x)+\frac{\varepsilon_+^2+\varepsilon^2}{\varepsilon_+\varepsilon}\mathrm{K}_{\frac{2}{3}}(z_p)-\frac{\omega}{\varepsilon}(\boldsymbol{\zeta}_-\cdot\mathbf{b})\mathrm{K}_{\frac{1}{3}}(z_p)\right\}\\
\tilde{G}_3 &= \bar{C}_0 d\varepsilon\left\{-\mathrm{K}_{\frac{2}{3}}(z_p)+\frac{\omega}{\varepsilon_+}(\boldsymbol{\zeta}_-\cdot\mathbf{b})\mathrm{K}_{\frac{1}{3}}(z_p)\right\}\\
\tilde{G}_1 &= -\bar{C}_0 d\varepsilon\frac{\omega}{\varepsilon_+}(\boldsymbol{\zeta}_-\cdot\mathbf{s})\mathrm{K}_{\frac{1}{3}}(z_p)\\
\tilde{G}_2 &= \bar{C}_0 d\varepsilon\left\{\left(\frac{\omega}{\varepsilon}\int_{z_p}^{\infty} dx \mathrm{K}_{\frac{1}{3}}(x)-\frac{\varepsilon_+^2-\varepsilon^2}{\varepsilon_+\varepsilon}\mathrm{K}_{\frac{2}{3}}(z_p)\right)(\boldsymbol{\zeta}_-\cdot\hat{\mathbf{v}})\right\},
\end{aligned}
\tag{B3}
$$

which can be rewritten in the form

$$
\begin{aligned}
d\tilde{W}^p(\boldsymbol{\xi},\boldsymbol{\zeta}_-) &= \frac{1}{2}(a_-+\boldsymbol{\zeta}_-\cdot\boldsymbol{b}_-)\\
a_- &= \bar{C}_0 d\varepsilon\left[\int_{z_p}^{\infty} dx \mathrm{K}_{\frac{1}{3}}(x)+\frac{\varepsilon_+^2+\varepsilon^2}{\varepsilon_+\varepsilon}\mathrm{K}_{\frac{2}{3}}(z_p)-\xi_3\mathrm{K}_{\frac{2}{3}}(z_p)\right]\\
\boldsymbol{b}_- &= -\bar{C}_0 d\varepsilon\left\{\xi_1\frac{\omega}{\varepsilon_+}\mathbf{s}\mathrm{K}_{\frac{1}{3}}(z_p)+\left(\frac{\omega}{\varepsilon}-\xi_3\frac{\omega}{\varepsilon_+}\right)\mathbf{b}\mathrm{K}_{\frac{1}{3}}(z_p)+\left[-\frac{\omega}{\varepsilon}\int_{z_p}^{\infty} dx \mathrm{K}_{\frac{1}{3}}(x)+\frac{\varepsilon_+^2-\varepsilon^2}{\varepsilon_+\varepsilon}\mathrm{K}_{\frac{2}{3}}(z_p)\right]\xi_2\hat{\mathbf{v}}\right\}.
\end{aligned}
\tag{B4}
$$

The final polarization vector of the produced electron resulting from the scattering process itself is $\boldsymbol{\zeta}_f^- = \frac{\boldsymbol{b}_-}{a_-}$, which determines the spin quantization axis for the produced electron $\boldsymbol{\zeta}_f^-$: $\boldsymbol{n}^- = \boldsymbol{\zeta}_f^-/|\boldsymbol{\zeta}_f^-|$.

b. Spin quantization axis for the produced positron

After taking the sum over electron polarizations,

$$
\begin{aligned}
d\bar{W}^p(\boldsymbol{\xi},\boldsymbol{\zeta}_+) &= \frac{1}{2}(\bar{G}_0+\xi_1\bar{G}_1+\xi_2\bar{G}_2+\xi_3\bar{G}_3),\\
\bar{G}_0 &= \bar{C}_0 d\varepsilon\left\{\int_{z_p}^{\infty} dx \mathrm{K}_{\frac{1}{3}}(x)+\frac{\varepsilon_+^2+\varepsilon^2}{\varepsilon_+\varepsilon}\mathrm{K}_{\frac{2}{3}}(z_p)+\frac{\omega}{\varepsilon_+}(\boldsymbol{\zeta}_+\cdot\mathbf{b})\mathrm{K}_{\frac{1}{3}}(z_p)\right\}\\
\bar{G}_3 &= \bar{C}_0 d\varepsilon\left\{-\mathrm{K}_{\frac{2}{3}}(z_p)-\frac{\omega}{\varepsilon}(\boldsymbol{\zeta}_+\cdot\mathbf{b})\mathrm{K}_{\frac{1}{3}}(z_p)\right\}\\
\bar{G}_1 &= \bar{C}_0 d\varepsilon\frac{\omega}{\varepsilon}(\boldsymbol{\zeta}_+\cdot\mathbf{s})\mathrm{K}_{\frac{1}{3}}(z_p)\\
\bar{G}_2 &= \bar{C}_0 d\varepsilon\left\{\left(\frac{\omega}{\varepsilon_+}\int_{z_p}^{\infty} dx \mathrm{K}_{\frac{1}{3}}(x)+\frac{\varepsilon_+^2-\varepsilon^2}{\varepsilon_+\varepsilon}\mathrm{K}_{\frac{2}{3}}(z_p)\right)(\boldsymbol{\zeta}_+\cdot\hat{\mathbf{v}})\right\},
\end{aligned}
\tag{B5}
$$

which can also be written as

$$
\begin{aligned}
d\bar{W}^p(\boldsymbol{\xi},\boldsymbol{\zeta}_+) &= \frac{1}{2}(a_++\boldsymbol{\zeta}_+\cdot\boldsymbol{b}_+)\\
a_+ &= \bar{C}_0 d\varepsilon\left\{\int_{z_p}^{\infty} dx \mathrm{K}_{\frac{1}{3}}(x)+\frac{\varepsilon_+^2+\varepsilon^2}{\varepsilon_+\varepsilon}\mathrm{K}_{\frac{2}{3}}(z_p)-\xi_3\mathrm{K}_{\frac{2}{3}}(z_p)\right\}\\
\boldsymbol{b}_+ &= \bar{C}_0 d\varepsilon\left\{\xi_1\mathrm{K}_{\frac{1}{3}}(z_p)\frac{\omega}{\varepsilon}\mathbf{s}+\left(\frac{\omega}{\varepsilon_+}-\xi_3\bar{C}_0 d\varepsilon\frac{\omega}{\varepsilon}\right)\mathbf{b}\mathrm{K}_{\frac{1}{3}}(z_p)+\xi_2\hat{\mathbf{v}}\left(\frac{\omega}{\varepsilon_+}\int_{z_p}^{\infty} dx \mathrm{K}_{\frac{1}{3}}(x)+\frac{\varepsilon_+^2-\varepsilon^2}{\varepsilon_+\varepsilon}\mathrm{K}_{\frac{2}{3}}(z_p)\right)\right\}.
\end{aligned}
\tag{B6}
$$

The final polarization vector of the produced positron resulting from the scattering process itself is $\boldsymbol{\zeta}_f^+ = \frac{\boldsymbol{b}_+}{a_+}$, which determines the spin quantization axis for the produced positron: $\boldsymbol{n}^+ = \boldsymbol{\zeta}_f^+/|\boldsymbol{\zeta}_f^+|$.

After taking the sum over positron and electron polarizations, we get the spin unresolved pair production probability:

$$dW_T^P(\boldsymbol{\xi}) = a_+. \tag{B7}$$

2. Polarization-resolved no-production probability

If a pair production event is rejected, then the photon polarization should also change due to the dependency of no-pair-production probability on photon polarization:

$$\begin{aligned} W^{NP}(\boldsymbol{\xi},\boldsymbol{\xi}') &= \frac{1}{2}(c^{NP} + \mathbf{d}^{NP}\cdot\boldsymbol{\xi}') \\ c^{NP} &= 1 - \int_0^\omega a_+ d\varepsilon\Delta t \\ \boldsymbol{d}^{NP} &= \boldsymbol{\xi}\left(1 - \int_0^\omega d\varepsilon\bar{C}_0\left[\int_{z_p}^\infty dx \mathrm{K}_{\frac{1}{3}}(x) \right.\right. \\ &\quad \left.\left. + \frac{\varepsilon_+^2+\varepsilon^2}{\varepsilon\varepsilon_+}\mathrm{K}_{\frac{2}{3}}(z_p)\right]\Delta t\right) \\ &\quad + \int_0^\omega d\varepsilon\bar{C}_0\hat{e}_3\mathrm{K}_{\frac{2}{3}}(z_p)\Delta t, \end{aligned} \tag{B8}$$

where $\hat{e}_3 = (0,0,1)$. The final polarization state of the photon after the no-pair-production step becomes $\boldsymbol{\xi}_f^{NP} = \boldsymbol{d}^{NP}/c^{NP}$, which defines a quantization axis for photon polarization: $\boldsymbol{n}^{NP} = \boldsymbol{\xi}_f^{NP}/|\boldsymbol{\xi}_f^{NP}|$.

The polarization induced by the no-pair-production process can be estimated as

$$\begin{aligned} \Delta\boldsymbol{\xi}^{NP} &= W^{NR}(\boldsymbol{\xi}_f^{NP} - \boldsymbol{\xi}_i) \\ &= \int_0^\omega d\varepsilon\bar{C}_0(\hat{e}_3 - (\boldsymbol{\xi}_i\cdot\hat{e}_3)\boldsymbol{\xi}_i)\mathrm{K}_{\frac{2}{3}}(z_p)\Delta t. \end{aligned} \tag{B9}$$

In our scheme, the intermediate gamma photons are linearly polarized with $\xi_3 \approx \pm 1$, such that the polarization of the photon is unchanged during the no-pair-production process, i.e. $\Delta\xi^{NP} \approx 0$. Therefore, no-pair-production polarization is trivial in this study.

3. Algorithm of event generation

a. Decide pair production event

At each simulation step, the pair production and the electron energy are determined by the probability of Eq. (B7), using the common stochastic procedure:

(1) Generate two random numbers $r_1, r_2 \in [0,1]$ with uniform probability.
(2) Compute the pair production probability $P(r_1) = dW_T^P(\boldsymbol{\xi}, r_1\omega)\Delta t$ for the given initial photon polarization $\boldsymbol{\xi}$, electron energy $\varepsilon = r_1\omega$, and positron energy $\varepsilon_+ = (1-r_1)\omega$.
(3) If $r_2 < P(r_1)$, then an e^+e^- pair is created. Otherwise, reject.

b. Decide the polarization of outgoing particles

Case 1: $P(r_1) > r_2$: pair production occurs. After each pair production, the spin of the produced electron (positron) is either parallel or antiparallel to $\boldsymbol{n}^-$ ($\boldsymbol{n}^+$) using the stochastic procedure with another random number $r_3 \in [0,1]$. With the given ε_-, ε_+ and photon polarization $\boldsymbol{\xi}$, compute the pair production probability $P_{\zeta_-\zeta_+} = dW^P(\boldsymbol{\xi},\boldsymbol{\zeta}_-,\boldsymbol{\zeta}_+)\Delta t$ with $\{\boldsymbol{\zeta}_-,\boldsymbol{\zeta}_+\} \in \{\uparrow,\downarrow\}$ indicating parallel or antiparallel with respective quantization axis.

(1) If $r_3 < P_{\downarrow\downarrow}$, then the electron is spin down with respect to $\boldsymbol{n}^-$, and the positron is spin down with respect to $\boldsymbol{n}^+$, i.e. $\boldsymbol{\zeta}_- = -\boldsymbol{n}^-$, $\boldsymbol{\zeta}_+ = -\boldsymbol{n}^+$.
(2) If $P_{\downarrow\downarrow} < r_3 < P_{\downarrow\downarrow} + P_{\downarrow\uparrow}$, then $\boldsymbol{\zeta}_- = -\boldsymbol{n}^-$ and $\boldsymbol{\zeta}_+ = \boldsymbol{n}^+$.
(3) If $P_{\downarrow\downarrow} + P_{\downarrow\uparrow} < r_3 < P_{\downarrow\downarrow} + P_{\downarrow\uparrow} + P_{\uparrow\downarrow}$, then $\boldsymbol{\zeta}_- = \boldsymbol{n}^-$ and $\boldsymbol{\zeta}_+ = -\boldsymbol{n}^+$.
(4) If $P_{\downarrow\downarrow} + P_{\downarrow\uparrow} + P_{\uparrow\downarrow} < r_3 < P_{\downarrow\downarrow} + P_{\downarrow\uparrow} + P_{\uparrow\downarrow} + P_{\uparrow\uparrow}$, then $\boldsymbol{\zeta}_- = \boldsymbol{n}^-$ and $\boldsymbol{\zeta}_+ = \boldsymbol{n}^+$.

Case 2: $P(r_1) < r_2$: pair production is rejected. The photon polarization state collapses into one of its basis states defined with respect to $\boldsymbol{n}^{NP}$:

(1) Generate another random number $r_4 \in [0,1]$.
(2) Compute the no-pair-production probability $P_{\boldsymbol{\xi}'} = W^{NP}(\boldsymbol{\xi},\boldsymbol{\xi}')$ for a given initial photon polarization $\boldsymbol{\xi}$. Here $\boldsymbol{\xi}' \in \{\uparrow,\downarrow\}$ indicates spin parallel or antiparallel with $\boldsymbol{n}^{NP}$.
(3) If $P_\uparrow/(P_\uparrow + P_\downarrow) > r_4$, then $\boldsymbol{\xi}' = \boldsymbol{n}^{NP}$. Otherwise, $\boldsymbol{\xi}' = -\boldsymbol{n}^{NP}$.

[1] E. Voutier, Physics potential of polarized positrons at the Jefferson Laboratory, Nucl. Theor. **33**, 142 (2014).

[2] F. E. Maas *et al.*, Measurement of Strange-Quark Contributions to the Nucleon's Form Factors at $Q^2 = 0.230$ $(\mathrm{GeV}/c)^2$, Phys. Rev. Lett. **93**, 022002 (2004).

[3] G. Moortgat-Pick, T. Abe, G. Alexander, B. Ananthanarayan, A. Babich, V. Bharadwaj, D. Barber, A. Bartl, A. Brachmann, S. Chen *et al.*, Polarized positrons and electrons at the linear collider, Phys. Rep. **460**, 131 (2008).

[4] D. T. Pierce and F. Meier, Photoemission of spin-polarized electrons from GaAs, Phys. Rev. B **13**, 5484 (1976).

[5] A. A. Sokolov and I. M. Ternov, On polarization and spin effects in the theory of synchrotron radiation, Sov. Phys. Dokl. **8**, 1203 (1964).

[6] V. Baier and V. Katkov, Radiational polarization of electrons in inhomogeneous magnetic field, Phys. Lett. **24A**, 327 (1967).

[7] Ya. S. Derbenev and A. M. Kondratenko, Polarization kinematics of particles in storage rings, Zh. Èksp. Teor. Fiz. **64**, 1918 (1973) [Sov. Phys . JETP **37**, 968 (1973)].

[8] P. Zitzewitz, J. Van House, A. Rich, and D. Gidley, Spin Polarization of Low-Energy Positron Beams, Phys. Rev. Lett. **43**, 1281 (1979).

[9] (Polarized) Positron Sources at the ILC, http://www.desy.de/gudrid/source/.

[10] G. Alexander, J. Barley, Y. Batygin, S. Berridge, V. Bharadwaj, G. Bower, W. Bugg, F.-J. Decker, R. Dollan, Y. Efremenko *et al.*, Observation of Polarized Positrons from an Undulator-Based Source, Phys. Rev. Lett. **100**, 210801 (2008).

[11] A. Mikhailichenko, G. Alexander, Y. Batygin, S. Berridge, V. Bharadwaj, G. Bower, W. Bugg, F.-J. Decker, R. Dollan, Y. Efrimenko *et al.*, The E166 experiment: Undulator-based production of polarized positrons, AIP Conf. Proc. **915**, 1095 (2007).

[12] T. Omori, M. Fukuda, T. Hirose, Y. Kurihara, R. Kuroda, M. Nomura, A. Ohashi, T. Okugi, K. Sakaue, T. Saito *et al.*, Efficient Propagation of Polarization from Laser Photons to Positrons through Compton Scattering and Electron-Positron Pair Creation, Phys. Rev. Lett. **96**, 114801 (2006).

[13] D. Abbott, P. Adderley, A. Adeyemi, P. Aguilera, M. Ali, H. Areti, M. Baylac, J. Benesch, G. Bosson, B. Cade *et al.*, Production of Highly Polarized Positrons using Polarized Electrons at MeV Energies, Phys. Rev. Lett. **116**, 214801 (2016).

[14] D. Scott, J. Clarke, D. Baynham, V. Bayliss, T. Bradshaw, G. Burton, A. Brummitt, S. Carr, A. Lintern, J. Rochford *et al.*, Demonstration of a High-Field Short-Period Superconducting Helical Undulator Suitable for Future TeV-Scale Linear Collider Positron Sources, Phys. Rev. Lett. **107**, 174803 (2011).

[15] J. W. Yoon, Y. G. Kim, I. W. Choi, J. H. Sung, H. W. Lee, S. K. Lee, and C. H. Nam, Realization of laser intensity over 10^{23} w/cm^2, Optica **8**, 630 (2021).

[16] The Vulcan facility, http://www.clf.stfc.ac.uk/Pages/The-Vulcan-10-Petawatt-Project.aspx.

[17] J. Zou *et al.*, Design and current progress of the Apollon 10 PW project, High Power Laser Sci. Eng. **3**, e2 (2015).

[18] CORELS facility in Korea, https://corels.ibs.re.kr.

[19] The Extreme Light Infrastructure (ELI), http://www.eli-beams.eu/en/facility/lasers/.

[20] Exawatt Center for Extreme Light Studies (XCELS), http://www.xcels.iapras.ru/.

[21] H. Chen, S. C. Wilks, J. D. Bonlie, E. P. Liang, J. Myatt, D. F. Price, D. D. Meyerhofer, and P. Beiersdorfer, Relativistic Positron Creation Using Ultraintense Short Pulse Lasers, Phys. Rev. Lett. **102**, 105001 (2009).

[22] H. Chen *et al.*, Relativistic Quasimonoenergetic Positron Jets from Intense Laser-Solid Interactions, Phys. Rev. Lett. **105**, 015003 (2010).

[23] H. Chen, F. Fiuza, A. Link, A. Hazi, M. Hill, D. Hoarty, S. James, S. Kerr, D. D. Meyerhofer, J. Myatt, J. Park, Y. Sentoku, and G. J. Williams, Scaling the Yield of Laser-Driven Electron-Positron Jets to Laboratory Astrophysical Applications, Phys. Rev. Lett. **114**, 215001 (2015).

[24] E. Liang, T. Clarke, A. Henderson, W. Fu, W. Lo, D. Taylor, P. Chaguine, S. Zhou, Y. Hua, X. Cen, X. Wang, J. Kao, H. Hasson, G. Dyer, K. Serratto, N. Riley, M. Donovan, and T. Ditmire, High e+/e- ratio dense pair creation with $10^{21} W.cm^{-2}$ laser irradiating solid targets, Sci. Rep. **5**, 13968 (2015).

[25] G. Sarri *et al.*, Generation of neutral and high-density electron-positron pair plasmas in the laboratory, Nat. Commun. **6**, 6747 (2015).

[26] G. Kotkin, H. Perlt, and V. Serbo, Polarization of high-energy electrons traversing a laser beam, Nucl. Instrum. Methods Phys. Res., Sect. A **404**, 430 (1998).

[27] P. Panek, J. Z. Kamiński, and F. Ehlotzky, Laser-induced compton scattering at relativistically high radiation powers, Phys. Rev. A **65**, 022712 (2002).

[28] G. L. Kotkin, V. G. Serbo, and V. I. Telnov, Electron (positron) beam polarization by Compton scattering on circularly polarized laser photons, Phys. Rev. ST Accel. Beams **6**, 011001 (2003).

[29] D. Y. Ivanov, G. Kotkin, and V. Serbo, Complete description of polarization effects in emission of a photon by an electron in the field of a strong laser wave, Eur. Phys. J. C **36**, 127 (2004).

[30] M. Boca, V. Dinu, and V. Florescu, Spin effects in nonlinear Compton scattering in a plane-wave laser pulse, Nucl. Instrum. Methods Phys. Res., Sect. B **279**, 12 (2012).

[31] D. V. Karlovets, Radiative polarization of electrons in a strong laser wave, Phys. Rev. A **84**, 062116 (2011).

[32] K. Krajewska and J. Z. Kamiński, Spin effects in nonlinear Compton scattering in ultrashort linearly-polarized laser pulses, Laser Part. Beams **31**, 503 (2013).

[33] D. Seipt, D. Del Sorbo, C. Ridgers, and A. Thomas, Theory of radiative electron polarization in strong laser fields, Phys. Rev. A **98**, 023417 (2018).

[34] S. Ahrens, H. Bauke, C. H. Keitel, and C. Müller, Spin Dynamics in the Kapitza-Dirac Effect, Phys. Rev. Lett. **109**, 043601 (2012).

[35] M. M. Dellweg, H. M. Awwad, and C. Müller, Spin dynamics in Kapitza-Dirac scattering of electrons from bichromatic laser fields, Phys. Rev. A **94**, 022122 (2016).

[36] M. M. Dellweg and C. Müller, Spin-Polarizing Interferometric Beam Splitter for Free Electrons, Phys. Rev. Lett. **118**, 070403 (2017).

[37] Y. S. Tsai, Laser+$e^- \to \gamma + e^-$ and laser+$\gamma \to e^+ + e^-$ as sources of producing circularly polarized γ and $e\pm$ beams, Phys. Rev. D **48**, 96 (1993).
[38] D. Y. Ivanov, G. Kotkin, and V. Serbo, Complete description of polarization effects in e^+e^- pair productionby a photon in the field of a strong laser wave, Eur. Phys. J. C **40**, 27 (2005).
[39] M. J. A. Jansen, J. Z. Kamiński, K. Krajewska, and C. Müller, Strong-field Breit-Wheeler pair production in short laser pulses: Relevance of spin effects, Phys. Rev. D **94**, 013010 (2016).
[40] A. Di Piazza, A. Milstein, and C. Müller, Polarization of the electron and positron produced in combined Coulomb and strong laser fields, Phys. Rev. A **82**, 062110 (2010).
[41] V. N. Baier, V. M. Katkov, and V. M. Strakhovenko, *Electromagnetic Processes at High Energies in Oriented Single Crystals* (World Scientific, Singapore, 1998).
[42] V. I. Ritus, Quantum effects of the interaction of elementary particles with an intense electromagnetic field, J. Sov. Laser Res. **6**, 497 (1985).
[43] V. N. Baier, Radiative polarization of electrons in storage rings, Sov. Phys. Usp. **14**, 695 (1972).
[44] D. Del Sorbo, D. Seipt, T. G. Blackburn, A. G. Thomas, C. D. Murphy, J. G. Kirk, and C. Ridgers, Spin polarization of electrons by ultraintense lasers, Phys. Rev. A **96**, 043407 (2017).
[45] D. Del Sorbo, D. Seipt, A. G. Thomas, and C. Ridgers, Electron spin polarization in realistic trajectories around the magnetic node of two counter-propagating, circularly polarized, ultra-intense lasers, Plasma Phys. Controlled Fusion **60**, 064003 (2018).
[46] Y.-F. Li, R. Shaisultanov, K. Z. Hatsagortsyan, F. Wan, C. H. Keitel, and J.-X. Li, Ultrarelativistic Electron Beam Polarization in Single-Shot Interaction with an Ultraintense Laser Pulse, Phys. Rev. Lett. **122**, 154801 (2019).
[47] Y.-F. Li, R. Shaisultanov, Y.-Y. Chen, F. Wan, K. Z. Hatsagortsyan, C. H. Keitel, and J.-X. Li, Polarized Ultrashort Brilliant Multi-GeV γ Rays via Single-Shot Laser-Electron Interaction, Phys. Rev. Lett. **124**, 014801 (2020).
[48] Y.-F. Li, Y.-Y. Chen, W.-M. Wang, and H.-S. Hu, Production of Hghly Polarized Positron Beams via Helicity Transfer from Polarized Electrons in a Strong Laser Field, Phys. Rev. Lett. **125**, 044802 (2020).
[49] Y.-Y. Chen, K. Z. Hatsagortsyan, C. H. Keitel, and R. Shaisultanov, Electron spin- and photon polarization-resolved probabilities of strong-field qed processes, Phys. Rev. D **105**, 116013 (2022).
[50] Y.-Y. Chen, P.-L. He, R. Shaisultanov, K. Z. Hatsagortsyan, and C. H. Keitel, Polarized Positron Beams via Intense Two-Color Laser Pulses, Phys. Rev. Lett. **123**, 174801 (2019).
[51] D. Seipt, D. D. Sorbo, C. P. Ridgers, and A. G. R. Thomas, Ultrafast polarization of an electron beam in an intense bichromatic laser field, Phys. Rev. A **100**, 061402 (2019).
[52] F. Wan, R. Shaisultanov, Y.-F. Li, K. Z. Hatsagortsyan, C. H. Keitel, and J.-X. Li, Ultrarelativistic polarized positron jets via collision of electron and ultraintense laser beams, Phys. Lett. B **800**, 135120 (2020).
[53] Y.-F. Li, R.-T. Guo, R. Shaisultanov, K. Z. Hatsagortsyan, and J.-X. Li, Electron Polarimetry with Nonlinear Compton Scattering, Phys. Rev. Appl. **12**, 014047 (2019).
[54] H.-H. Song, W.-M. Wang, and Y.-T. Li, Dense Polarized Positrons from Laser-Irradiated Foil Targets in the QED Regime, Phys. Rev. Lett. **129**, 035001 (2022).
[55] Y.-F. Li, Y.-Y. Chen, K. Z. Hatsagortsyan, and C. H. Keitel, Helicity Transfer in Strong Laser Fields via the Electron Anomalous Magnetic Moment, Phys. Rev. Lett. **128**, 174801 (2022).
[56] Q. Ma, Y. Tang, J. Yu, Y. Shou, X. Wu, and X. Yan, Production of Multioriented Polarization for Relativistic Electron Beams via a Mutable Filter for Nonlinear Compton Scattering, Phys. Rev. Appl. **19**, 014058 (2023).
[57] Z. Gong, K. Z. Hatsagortsyan, and C. H. Keitel, Retrieving Transient Magnetic Fields of Ultrarelativistic Laser Plasma via Ejected Electron Polarization, Phys. Rev. Lett. **127**, 165002 (2021).
[58] Z. Gong, K. Z. Hatsagortsyan, and C. H. Keitel, Deciphering *in situ* electron dynamics of ultrarelativistic plasma via polarization pattern of emitted γ-photons, Phys. Rev. Res. **4**, L022024 (2022).
[59] Z. Gong, K. Z. Hatsagortsyan, and C. H. Keitel, Electron Polarization in Ultrarelativistic Plasma Current Filamentation Instabilities, Phys. Rev. Lett. **130**, 015101 (2023).
[60] A. Di Piazza, K. Z. Hatsagortsyan, and C. H. Keitel, Strong Signatures of Radiation Reaction Below the Radiation-Dominated Regime, Phys. Rev. Lett. **102**, 254802 (2009).
[61] J.-X. Li, K. Z. Hatsagortsyan, B. J. Galow, and C. H. Keitel, Attosecond Gamma-Ray Pulses via Nonlinear Compton Scattering in the Radiation-Dominated Regime, Phys. Rev. Lett. **115**, 204801 (2015).
[62] A. Di Piazza, C. Müller, K. Z. Hatsagortsyan, and C. H. Keitel, Extremely high-intensity laser interactions with fundamental quantum systems, Rev. Mod. Phys. **84**, 1177 (2012).
[63] Y.-N. Dai, B.-F. Shen, J.-X. Li, R. Shaisultanov, K. Z. Hatsagortsyan, C. H. Keitel, and Y.-Y. Chen, Photon polarization effects in polarized electron–positron pair production in a strong laser field, Matter Radiat. Extremes **7**, 014401 (2022).
[64] V. Bargmann, L. Michel, and V. L. Telegdi, Precession of the Polarization of Particles Moving in a Homogeneous Electromagnetic Field, Phys. Rev. Lett. **2**, 435 (1959).
[65] M. W. Walser, D. J. Urbach, K. Z. Hatsagortsyan, S. X. Hu, and C. H. Keitel, Spin and radiation in intense laser fields, Phys. Rev. A **65**, 043410 (2002).
[66] Y.-F. Li, Y.-Y. Chen, K. Z. Hatsagortsyan, A. Di Piazza, M. Tamburini, and C. H. Keitel, Strong signature of one-loop self-energy in polarization resolved nonlinear Compton scattering, Phys. Rev. D **107**, 116020 (2023).
[67] E. Esarey, C. Schroeder, and W. Leemans, Physics of laser-driven plasma-based electron accelerators, Rev. Mod. Phys. **81**, 1229 (2009).
[68] A. Gonoskov, S. Bastrakov, E. Efimenko, A. Ilderton, M. Marklund, I. Meyerov, A. Muraviev, A. Sergeev, I. Surmin, and E. Wallin, Extended particle-in-cell schemes for physics in ultrastrong laser fields: Review and developments, Phys. Rev. E **92**, 023305 (2015).
[69] Y. Tang, Z. Gong, J. Yu, Y. Shou, and X. Yan, Radiative polarization dynamics of relativistic electrons in an intense electromagnetic field, Phys. Rev. A **103**, 042807 (2021).